Nonlinear Dynamics in Nanomechanical Oscillators

Ronen Almog

Nonlinear Dynamics in Nanomechanical Oscillators

RESEARCH THESIS

SUBMITTED IN PARTIAL FULFILLMENT OF THE REQUIREMENTS FOR THE DEGREE OF DOCTOR OF PHILOSOPHY

Ronen Almog

SUBMITTED TO THE SENATE OF THE TECHNION - ISRAEL INSTITUTE OF TECHNOLOGY

TEVET 5767 HAIFA JANUARY 2007

thispagestyleempty

This Research Thesis Was Done Under The Supervision of Doctor Eyal Buks in the Faculty of Electrical Engineering

The Generous Financial Help of Intel Corp., Applied Materials, the Israel-US Binational Science Foundation (BSF grant no. 2004362), Henri Gutwirth Fund, the Russell Berrie Nanotechnology Institute and the Technion is Gratefully Acknowledged.

Acknowledgments

I would like to express my special gratitude to my supervisor, Dr. Eyal Buks, for believing in me and supporting me through out the research, with endless patience but with high expectations. His devotion to the research, along with his deep knowledge and wise guidance, set the basis on which this research was built.

I would like to express my special gratitude to Oleg Shtempluck who had a major part in the success of this research. I would like to thank Bernard Yurke, Oded Gottlieb and my group members - Stav, Eran and Baleegh for helpful discussions.

I would like to thank all the employees of the microelectronic institute, who were always there for me when needed, with an advice or a supporting hand. I would like to thank Alex bekker, Boris Levit and Vladimir Smulakovsky whose help had a major contribution to the successful setup of the optical detection system.

Finally, last but not least, I would like to thank my wife Sarit and my parents Nissim and Shoshana, for their love, support and understanding.

Contents

List of Figures

Abstract

Micro/Nanoelectromechanical resonators are widely employed for applications such as sensing, switching, and filtering. In particular, such resonators can be used for ultra-sensitive force/mass measurements. A possible technique to improve signal to noise ratio in such devices is to implement an on-chip mechanical amplification.

In this work we have focused on the understanding of nonlinear dynamics in such devices and the development of novel amplification schemes. Two mechanisms of amplification were experimentally studied: (a) Small signal amplification in a bifurcating dynamical system, exploiting its high sensitivity to fluctuations near its bifurcation point. This amplification mechanism is known as Bifurcation Amplification.
(b) Stochastic resonance, in which an appropriate amount of noise is used to amplify a periodic signal acting on a bistable nonlinear system.

In the first amplification mechanism we have studied mechanical amplification and noise squeezing in a nonlinear nanomechanical resonator driven by an intense pump near its dynamical bifurcation point, namely, the onset of Duffing bistability. We have employed bifurcation amplification for the first time in nanomechanical resonators to demonstrate high signal gain, phase sensitive amplification and noise squeezing. Phase sensitive amplification is achieved by a homodyne detection scheme, where the output signal could be either amplified or deamplified, depending on a local oscillator phase.

In the second amplification mechanism, we have studied stochastic resonance in a nonlinear bistable nanomechanical resonator. The resonator is tuned to its bistability region by an intense pump near a point of equal transition rates between its two metastable oscillation states. The pump is amplitude modulated, inducing thus modulation of the activation barrier between the states. When noise is added to the excitation, the resonator's response exhibits noise dependent amplification.

The oscillator under study consists of a nonlinear doubly clamped nanomechanical AuPd beam, excited capacitively by an adjacent gate electrode and its vibrations are detected optically.

The work included fabrication, process development, setup of an optical system for displacement detection, measurements, analysis, and theory for selected subjects.

Glossary

Acronyms:

AM	Amplitude modulation
EBL	Electron beam lithography
ECR	Electron cyclotron resonance
EOM	Equation of motion
IF	Intermediate frequency
IM	Intermodulation
IR	Infra red
KOH	Potassium Hydroxide
LO	Local oscillator
LPF	Low-pass filter
MEMS	Microelectromechanical system
MRFM	Magnetic resonance force microscopy
NA	Network analyzer
NEMS	Nanoelectromechanical system
NMBA	Nanomechanical bifurcation amplifier
PD	Photodetector
PSA	Phase sensitive amplification
PMMA	PolyMethylMethAcrylate
PCB	Printed circuit board
SA	Spectrum Analyzer
SEM	Scanning electron microscope
SNR	Signal to noise ratio
SR	Stochastic resonance
RF	Radio frequency
VHF	Very high frequency

List of Symbols and abbreviation:

CF_4	Carbon tetrafluoride
O_2	Oxygen
Si	Silicon
Si_3N_4	Silicon Nitride
SiO_2	Silicon Oxide
Au	Gold
AuPd	Gold Paladium
ω_0	(Angular) Resonance frequency
ω	(Angular) Arbitrary frequency
ω_p	(Angular) Pump frequency
ω_s	(Angular) Signal frequency
ω_i	(Angular) Idler frequency
f_p	Pump force amplitude
f_s	Signal force amplitude
f_c	Critical force amplitude
V_p	Pump voltage
V_s	Signal voltage
V_{dc}	DC voltage
a_p	Displacement complex amplitude at the pump frequency
a_s	Displacement complex amplitude at the signal frequency
a_i	Displacement complex amplitude at the idler frequency
σ	Detuning
σ_c	Critical detuning
δ	Frequency difference
δm	Mass change
S_x	Displacement spectral power density
S_{Vnoise}	Voltage noise spectral density
S_{Fn}	Input noise spectral density

T	Temperature
Q	Quality factor
l	Length
t	Thickness
w	Width
d	Gap
m_{eff}	Effective mass
ρ	Specific density
A	Beam's cross section
$F(t)$	External force per unit mass
x	Displacement
μ	Damping constant
κ	Cubic nonlinear constant
Φ_{LO}	Local oscillator's phase
M	Mixing constant
R	Spectral density at the mixer's output
k_B	Boltzmann's constant
V_{MO}	Mixer's output voltage
V_{LO}	Local oscillator's output voltage
ζ	nonlinearity parameter
β	nonlinear damping constant
p	measure of the nonlinear damping relative strength
γ	Hamiltonian coupling constant, linear damping
γ_3	Hamiltonian coupling constant, nonlinear damping
K	Hamiltonian nonlinear cubic constant
f	Force complex amplitude
A	Anihilation operator
G	Amplification
Bp	Bifurcation point
S_h	High displacement amplitde state
S_l	Low displacement amplitde state
$\Gamma(D)$	Transition rate betwenn states
D	Noise intensity
I	Voltage noise intensity
ΔU	Activiation barrier
A_{mod}	Modulation amplitude
Ω	Modulation frequency
η_k	Spectral amplification
τ	Time difference
λ	Laser wavelength

Chapter 1

Introduction

Micro/Nanoelectromechanical resonators play a key role in microdevices for applications such as sensing, switching, and filtering [1]-[2] and are widely employed for ultra-sensitive force/mass measurements. Among these are devices for zeptogram scale mass sensing [5]-[16], single electron spin detection [17], and devices for RF communication [18].

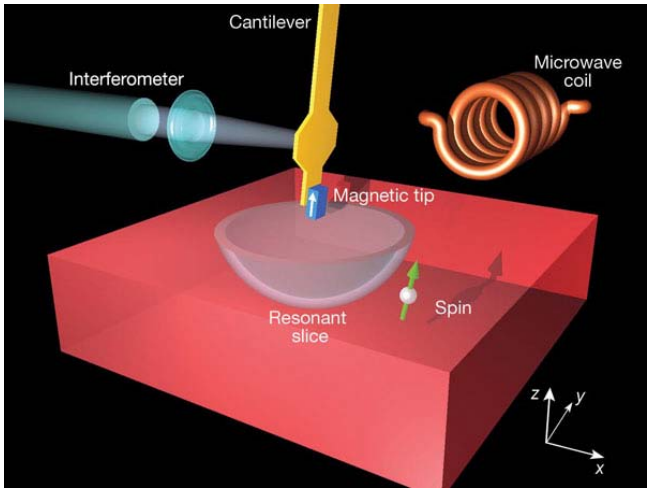

Figure 1.1: An example of an ultra-sensitive force measurement. A magnetic tip at the end of an ultrasensitive silicon cantilever is positioned approximately 125 nm above a polished SiO2 sample containing a low density of unpaired electron spins. The resonant slice represents those points in the sample where the field from the magnetic tip (plus an external field) matches the condition for magnetic resonance. As the cantilever vibrates, the resonant slice swings back and forth through the sample causing cyclic adiabatic inversion of the spin. The cyclic spin inversion causes a slight shift of the cantilever frequency owing to the magnetic force exerted by the spin on the tip. Spins as deep as 100 nm below the sample surface can be probed. The figure is taken from ref. [17].

In the first example, Very High Frequency (VHF) nanoelectromechanical system (NEMS) provide unprecedented sensitivity for inertial mass sensing. Such sensors promise a broad range of applications, from ultra-sensitive mass spectrometers that can be used to detect hazardous molecules, through biological applications at the level of a single DNA base-pair, to the study of fundamental questions such as the interaction of a single pair of molecules. In these devices, mass detection is achieved by monitoring the resonance frequency ω_0 of one of the modes of a nanomechanical resonator. The dependence of ω_0 on the effective mass m allows for sensitive detection of additional mass being adsorbed on the surfaces of the resonator. In such mass detectors the adsorbent molecules are anchored to the resonator surface either by Van der-Waals interaction, or by covalent bonds to linker molecules that are attached to the surface. Various analytes were used in those experiments, including alcohol and explosive gases, biomolecules, single cells, DNA molecules, and alkane chains. Currently, the smallest detectable mass change is $\delta m \simeq 0.4 \times 10^{-21}\,\mathrm{kg}$ [3], achieved by using a $4\,\mu$m long silicon beam with a resonance frequency $\omega_0/2\pi = 10\,\mathrm{MHz}$, a quality factor Q of about $2,500$, and total mass $m \simeq 5 \times 10^{-16}\,\mathrm{kg}$. In a recent experiment Ilic *et al.* [4] succeeded to measure a single DNA molecule of about $1,600$ base pairs, which corresponds to $\delta m \simeq 1.6 \times 10^{-21}\,\mathrm{kg}$, by using a silicon nitride cantilever, and employing an optical detection scheme.

The Caltech group [5], demonstrated real time *in situ* measurements with mass noise floor of approximately 20 zg and best mass resolution corresponds to approximately 7 zg, equivalent to 30 xenon atoms. NEMS can ultimately provide inertial mass sensing of individual intact, electrically neutral macromolecules with 1 amu resolution.

In the second example, the IBM group detected an individual electron spin by Magnetic Resonance Force Microscopy (MRFM). MRFM is based on the detection of the magnetic force between a ferromagnetic tip attached to a micromechanical cantilever and spins in a sample. The measurement method is demonstrated in Fig. 1.1.

In the third example, the Nguyen group utilized high Q's ($>10^4$) micromachined vibrating resonators as integrated circuit-compatible tanks to be used as low phase-noise oscillators and highly selective filters for communications subsystems.

There are three common characteristics to the above examples:
1) Ultra-sensitive displacement detection is needed.
2) They all operate in noisy environment
3) The nonlinear regime is easily accessible.

Understanding the nonlinear dynamics in such devices is highly important, both

for applications and for basic research [19]-[28]. The relatively small force needed for driving a microresonator into the nonlinear regime is usually easily accessible, enabling a variety of useful applications such as frequency mixing [29] and frequency synchronization [30].

Since nano-scale displacement detection is highly challenging, it is desirable to implement an on-chip mechanical amplification mechanism in order to improve signal to noise ratio. Previously, mechanical amplification and thermomechanical noise squeezing in microresonators have been achieved using parametric amplification [31]−[32].

In the present work [33]-[36], our goals were to investigate the nonlinear regime of nanomechanical resonators and to use the nonlinear regime in order to implement new mechanical amplification schemes.

1.1 Bifurcation Amplification

Our first amplification scheme is based on a bifurcating dynamical system, exploiting its high sensitivity to fluctuations near its bifurcation point. A driven nonlinear system operating close to bifurcation, namely, close to transition between different stability zones, is extremely sensitive to external perturbations [37]-[46]. Kirt Wiesenfeld was, seemingly, the first who studied the phenomenon of noise amplification near bifurcation threshold [37]. His analysis of prebifurcation noise amplification demonstrated unlimited growth of fluctuations in the immediate vicinity of the bifurcation point. Prebifurcation noise amplification might be an effective diagnostic instrument for a nonlinear system (so named "noisy precursor" of bifurcation). This amplification scheme has been used lately for quantum measurements of superconducting qubits [47].

In our case, we use the onset of bistability in a nanomechanical Duffing resonator as the bifurcation point. In a Duffing resonator, above some critical driving amplitude, the response becomes a multi-valued function of the frequency in some finite frequency range, and the system becomes bistable with jump points in the frequency response [48, 49]. We show theoretically and experimentally that this can be exploited for both amplification of small signals and for noise reduction ("noise squeezing") in nanomechanical resonators.

1.2 Stochastic Resonance

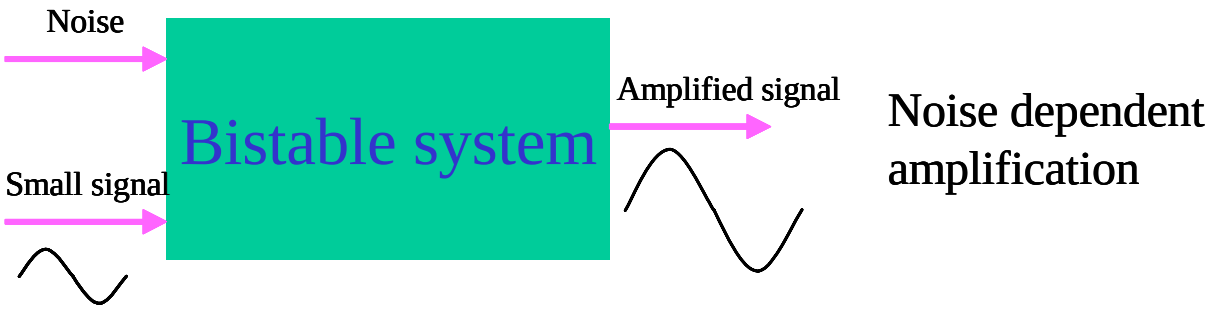

Figure 1.2: Illustration of stochastic resonance. An appropriate amount of noise is used to amplify a periodic signal acting on a bistable nonlinear system. The output signal exhibit noise dependent amplification.

Our second amplification scheme is based on Stochastic Resonance (SR) [51]−[53]. SR is a phenomenon in which a nonlinear system is subjected to a periodic signal so weak as to be normally undetectable, but it becomes detectable due to a cooperative effect between the weak deterministic signal and wide band stochastic noise (as illustrated in Fig. 1.2). In SR, the signal-to-noise ratio of a nonlinear device is maximized for a moderate value of noise intensity. It often occurs in bistable systems with subthreshold (due to an activation energy or barrier) inputs. The system response is driven by the combination of the two forces (small signal and noise) that compete/cooperate to make the system switch between the two stable states. For low noise intensities, the signal does not cause the device to cross threshold, so the output is a weak signal. For large noise intensities, the output is dominated by the noise, also leading to a low signal-to-noise ratio. For moderate intensities, the noise allows the signal to reach threshold, but the noise intensity is not so large as to swamp it. In this case, there can exist exactly one switch per half period accompanied by a maximum in the signal-to-noise ratio. Thus, a plot of signal-to-noise ratio as a function of noise intensity exhibit a peak for a moderate noise intensity. SR has been discovered and proposed for the first time in 1981 to explain the periodic recurrence of ice ages. Since then, the same principle has been applied in a wide variety of systems. SR has been demonstrated experimentally in electrical, optical, and superconducting systems, [54]−[58] as well as successfully explaining neurophysiological processes in neuronal systems [59]−[60]. Nowadays SR is commonly invoked when noise and nonlinearity cooperate to increase the system response. SR could be used as an amplification mechanism in nanomechanical devices in order to improve force detection sensitivity [61]−[62].

The thesis consists of the following parts.

Ch. 2 describes the sample layout, the fabrication process, the experimental setup together with sensitivity measurement and frequency response measurements.

Ch. 3 presents the theory of high intermodulation gain near the bifurcation point of a Duffing resonator and noise squeezing.

Ch. 4 presents the experimental investigation of the intermodulation gain near the bifurcation point of the nanomechanical oscillator.

Ch. 5 presents the experimental investigation of phase sensitive amplification and noise squeezing.

Ch. 6 presents the experimental investigation of stochastic resonance in our nanomechanical oscillator.

The last chapter, Ch. 7, concludes with a summary and suggests further research directions.

The appendix deals with nonlinear dissipation and includes our article - "Nonlinear Damping in Nanomechanical Beam Oscillator".

Chapter 2

The experimental Setup

2.1 Sample Description

The investigated device consists of a doubly clamped AuPd beam serving as a nanomechanical resonator excited capacitively by an adjacent gate electrode. Fig. 2.1 shows a typical device, consisting of two suspended nanomechanical resonators, centered around a wide gate electrode. Each resonator (beam) is of length l=100μm, width w=0.6μm, and thickness t=0.25μm, and the gap between the beams and the gate electrode is $d = 4\mu m$ gap. The gate electrode width is $10\mu m$. The quality factor (at 10^{-5} torr) is $Q \approx 2000$ and the resonance frequency $\omega_0/2\pi$ of the in-plane fundamental mode is around 500 kHz.

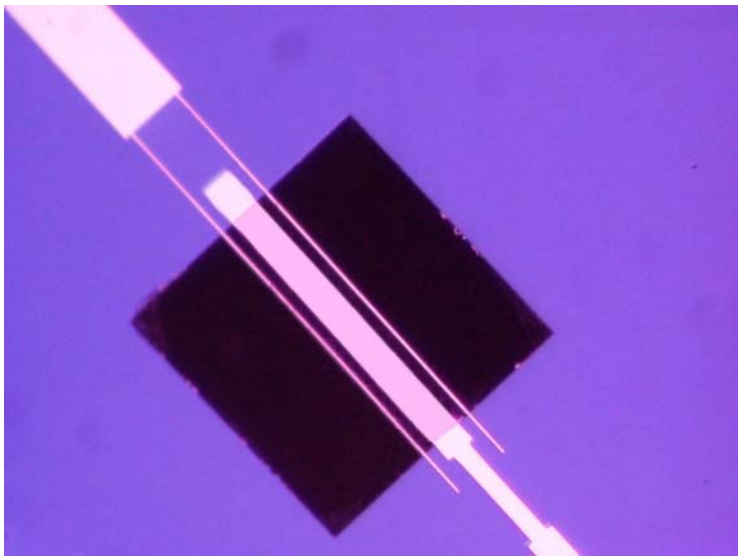

Figure 2.1: An optical image of the device (×1000 magnification). The black square hole is the place of the etched membrane, 100μm x 100μm in size.

Here the basic elastic properties and the dynamics of such a resonator is presented, based on the work done by Eyal Buks [63]−[65].

The equation of the in-plane motion of the beam is given by

$$\frac{\partial^2 y}{\partial x^2} - \zeta^2 l^2 \frac{\partial^4 y}{\partial x^4} = (\rho A/T)\frac{\partial^2 y}{\partial t^2} - \tilde{F}/T \tag{2.1}$$

where y is the transversal displacement along the longitudinal coordinate x. $\zeta^2 = EAw^2/12Tl^2$, with E being Young's modulus, $A = wt$ is the area of the beam's cross section ($w-$ width, $t-$thickness), T is the tension, ρ is the mass density, and $\tilde{F}$ is the density of the external force [66]. The clamping of the beam on both sides is taken into account using the boundary condition $y(\pm l/2) = (\partial y/\partial x)(\pm l/2) = 0$. The dimensionless parameter ζ indicates the relative effect of stiffness compared with tension on the dynamics of the beam. As we shall see below, $\zeta << 1$ and we can expand the resonance frequencies f_n of the system in powers of ζ. To second order we find

$$f_n = n f_0[1 + 2\zeta + (4 + n^2\pi^2/2)\zeta^2], \tag{2.2}$$

where $f_0 = \sqrt{T/\rho A}/2l$. The equally spaced spectrum obtained for the case $\zeta = 0$ is the same as for a stiffness-free beam (string) with boundary conditions $y(\pm l/2) = 0$. By a measurement of the frequencies of the first four modes [64], it was found that $\zeta < 0.015$, while measurement of the beam's deflection inside a scanning electron microscope, yields an estimated value $\zeta \approx 0.01$. This value and the other known parameters allow estimating Young's modulus $E \simeq 8 \times 10^{10}\,\mathrm{N/m^2}$. This value shows reasonable agreement with previous measurements of E in films of evaporated gold.

In our experiment we are interested only in the dynamics of the fundamental mode where the resonator is excited capacitively by an adjacent gate electrode. The motion of the fundamental mode could be modeled by a lumped system of mass, spring and capacitor.

When nonlinearity is taken into account to lowest order [49],[50], the nonlinear dynamics of the fundamental mode of a doubly clamped beam excited by an external force per unit mass $F(t)$ can be described by a Duffing oscillator equation for a single degree of freedom x (the displacement of the center of the beam in the fundamental mode)

$$\ddot{x} + 2\mu\dot{x} + \omega_0^2(1 + \kappa x^2)x = F(t), \tag{2.3}$$

where μ is the damping constant, $\omega_0/2\pi$ is the resonance frequency of the fundamental mode of the oscillator and κ is the cubic nonlinear constant.

We take into account only the first nonlinear term $\kappa\omega_0^2 x^3$- assuming an elastic

force derived from a symmetric potential, the force have to be an odd function. For small amplitudes, the nonlinearity originates from the axial stress which increases the beam stiffness ($\kappa > 0$) [50]. For higher amplitudes, however, the contribution of the applied electric force, which tend to soften the beam, becomes dominant.

The capacitance between the beam and the static gate electrode is $C(x) = C_0/(1 - \frac{x}{d})$ where d is the capacitor gap and C_0 is the initial capacitance. The electric force $F(t)$ is given by $F(t) = -dU_{sys}/dx = d(\frac{1}{2}CV^2)/dx$, where V is the applied voltage and $U_{sys} = -\frac{1}{2}CV^2$ is the electrical energy of the system, taking into account the work done by the source. In our case $x/d = 0.1 << 1$ thus $F(t) \approx \frac{1}{2d}C_0V^2$. The applied voltage is of the form $V{=}V_{dc} + V_p \cos\omega_p t$ where $V_{dc} >> V_p$ ($V_{dc}/V_p \geq 200$ in our experiment) to ensure a dominant excitation at ω_p and a negligible excitation at $2\omega_p$.

Generally, for resonators driven using a voltage applied to a side electrode, Eq. 3.1 should contain additional parametric terms [31],[68]. In our case however, the prefactors of these parametric terms are at least one order smaller below threshold and thus negligible.

2.2 The Fabrication Process

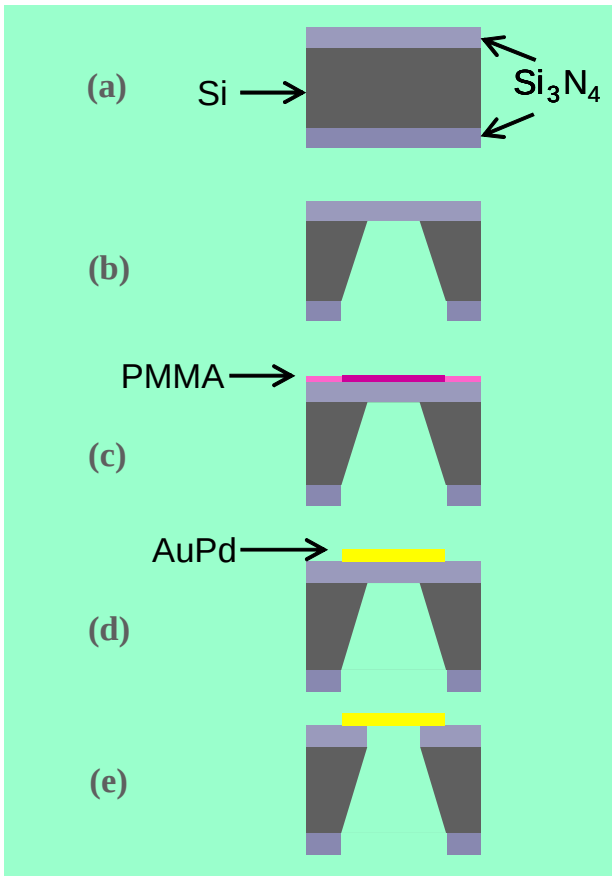

Figure 2.2: The fabrication process. The device is fabricated using a bulk micromachining process. In the first step, a suspended membrane of Si_3N_4 is formed. Next, a gold beam is fabricated on top of the membrane. Finally, the membrane is etched, leaving the beam suspended. The Si wafer thickness is 525 μm and the Si_3N_4 layer thickness is 100 nm.

The resonators are fabricated using a bulk micro-machining process together with electron beam lithography [63]. The bulk micromachining process employed for sample fabrication is described in Fig. 2.2.

Step 1 - we begin the process with a double side polished Si wafer with 100 nm layer of Si_3N_4 on both sides. In the first step, photolithography is used to clear out a square hole in the nitride on the backside.

Step 2 - the high selectivity and anisotropic etching properties of KOH etch are employed to form the structure shown in Fig. 2.2 - panel b, a 100 μm square of Si_3N_4 suspended membrane on the front side of the wafer. This membrane is to be used as the sacrificial layer for the suspended gold beam.

Step 3 - PMMA is deposited on the front side of the wafer and the device pattern is written in the PMMA using electron beam lithography (EBL), (Fig. 2.2 - panel c).

Step 4 - AuPd is evaporated on the front side of the wafer, followed by a lift-off process (Fig. 2.2 - panel d).

Step 5 -the Si_3N_4 membrane is removed using electron cyclotron resonance (ECR) plasma etch with CF_4/O_2 gas mixture bombarding the back side of the sample (Fig. 2.2 - panel e).

Step 6 - the sample is mounted on a PCB followed by wire-bonding (Fig. 2.3).

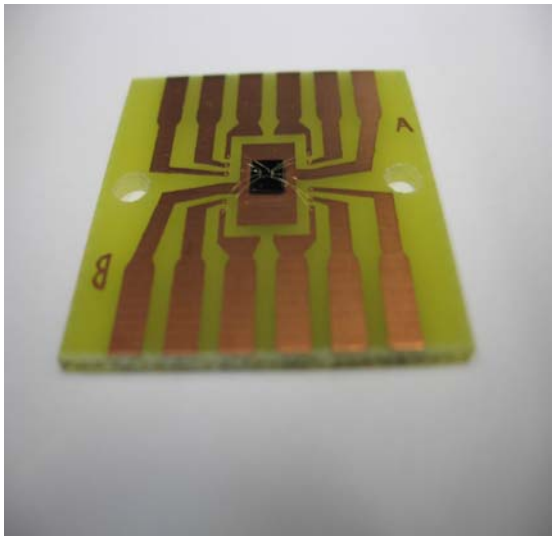

Figure 2.3: A sample mounted on a PCB.

2.3 The Measurement System

The measurement system is shown in Fig. 2.4. The resonator is excited by two sources (pump and small test signal or noise) and its vibrations are detected optically using a knife-edge technique [67]. The device is located close to the focal point of a lensed fiber which is used to focus laser light (IR laser operating at wavelength $\lambda = 1550\,\text{nm}$ and power of $20\,\text{mW}$) at the beam and to collect the reflected light back to the fiber and to a photodetector (PD). The PD signal is amplified, and measured by a spectrum/network analyzer. The measurement is done in vacuum (10^{-5} torr, inside the chamber of a scanning electron microscope) and at room temperature.

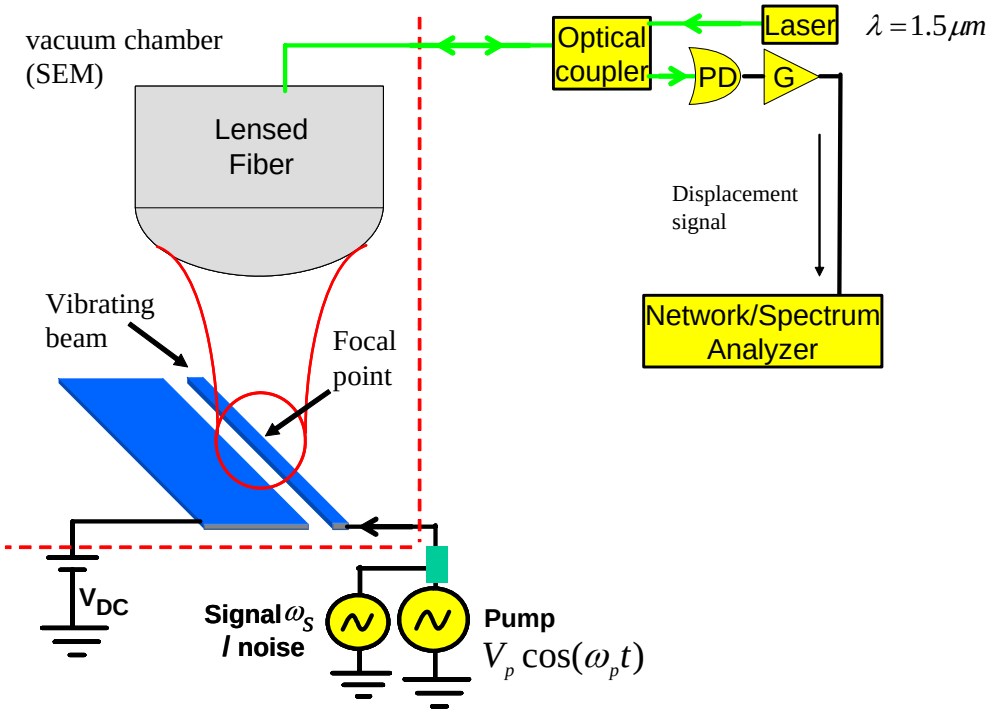

Figure 2.4: The measurement system. The resonator's vibration are detected optically.

2.4 Sensitivity Measurement

In order to find the measurement system sensitivity (noise floor), we disconnect the external sources and measure the spectrum of the thermal excitation (Brownian motion) of the fundamental mode of the beam. The measured thermal peak is shown in Fig. 2.5. Theoretically, the spectral power density of the displacement noise of the

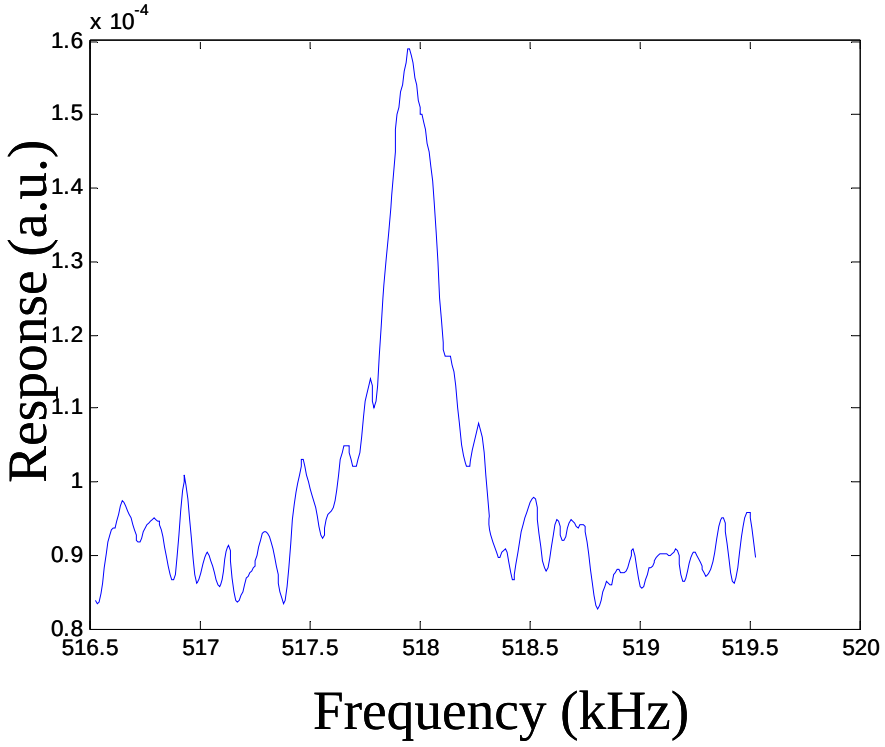

Figure 2.5: Spectral measurement of the thermal excitation of the fundamental mode of the beam.

center of the beam around the fundamental frequency is given by

$$S_x(\omega) = \frac{\omega_0 k_B T}{\pi Q m_{eff}[(\omega^2 - \omega_0^2)^2 + (\omega_0\omega/Q)^2]}, \tag{2.4}$$

where Q is the quality factor, $m_{eff} = \rho A l/2$ is the effective mass, T is the temperature, ρ is the specific density of the beam and A its cross section. The known parameters of the beam allow determination of the scaling factor translating the signal of the spectrum analyzer to actual displacement noise. Using this factor and the signal to noise ratio of the data in the figure, we find the noise floor of our displacement detection scheme (mainly due to the photodetector) to be $S_x(\omega) = 3.7\times10^{-13}\,\mathrm{m}/\,\mathrm{Hz}^{1/2}$ [64].

2.5 Frequency response

As a first step before any measurement, we characterize the frequency response of the device. This is achieved by sweeping the external force frequency upward and back downward for different constant excitation amplitudes Vp, without additional small signal or noise. Typical response curves are shown in Fig. 2.6. The inset shows hysteresis response for $Vp = 90\,\mathrm{mV}$.

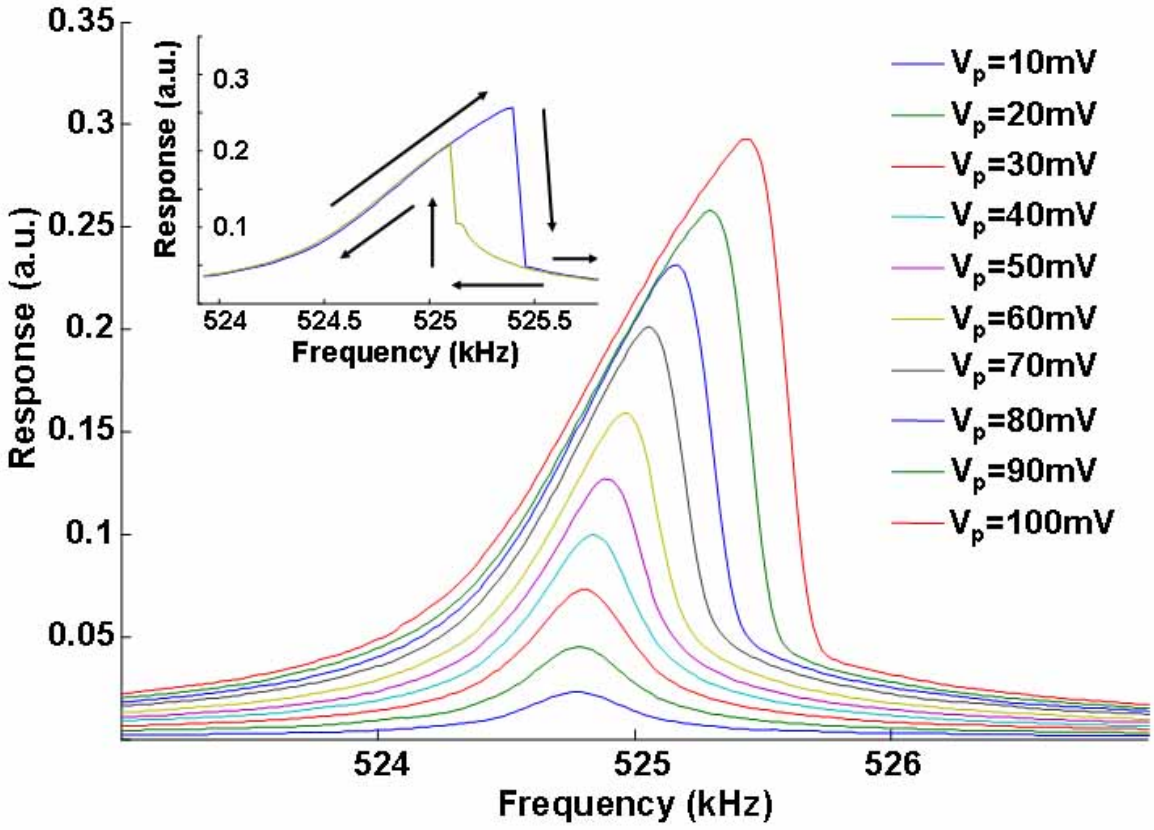

Figure 2.6: Typical frequency response curves for various excitation voltages Vp and upward frequency scan. The inset shows hysteresis response for $Vp = 90\,\mathrm{mV}$.

Chapter 3

Theory

3.1 The Nonlinear Equation of Motion

As was stated above in Eq. 2.3, the relevant equation of motion is

$$\ddot{x} + 2\mu\dot{x} + \omega_0^2(1 + \kappa x^2)x = F(t). \tag{3.1}$$

The external force $F(t) = f_p \cos(\omega_p t) + f_s \cos(\omega_s t + \varphi)$ composed of an intense *pump* with amplitude f_p, frequency ω_p, and a weak force (called *signal*) with amplitude f_s, frequency ω_s and relative phase φ, where $f_s << f_p$. We define the detuning $\sigma \equiv \omega_p - \omega_0$ and $\delta \equiv \omega_s - \omega_p$ where $\sigma, \delta << \omega_0$.

In case that $F(t)$ consists of pump only, the resonator dynamics depends on a critical amplitude f_c as demonstrated in Fig. 3.1, which shows three different frequency response curves [48]. In the subcritical case when $f_p < f_c$, the response is a tilted Lorentzian. In the critical case when $f_p = f_c$, the response has a point with infinite slope and the resonator dynamics is in the onset of hysteresis and bistability. When $f_p > f_c$ the response becomes a multi-valued function of the frequency in some finite frequency range, and the system becomes bistable with jump points in the frequency response. In the language of dynamical systems, this critical point is called bifurcation point (a saddle-node bifurcation point in this case).

When the external force consists of pump and a signal, the resonator's displacement has spectral components at ω_p, ω_s, and at the intermodulations $\omega_p \pm k\delta$ where k is an integer (see Fig. 3.2). The one at frequency $\omega_i = \omega_p - \delta$ is called the *idler* component, as in nonlinear optics.

In order to find a solution to Eq. 3.1 in the general case, we write $x(t)$ as

$$x(t) = \frac{1}{2} e^{i\omega_p t} A(t) + c.c \tag{3.2}$$

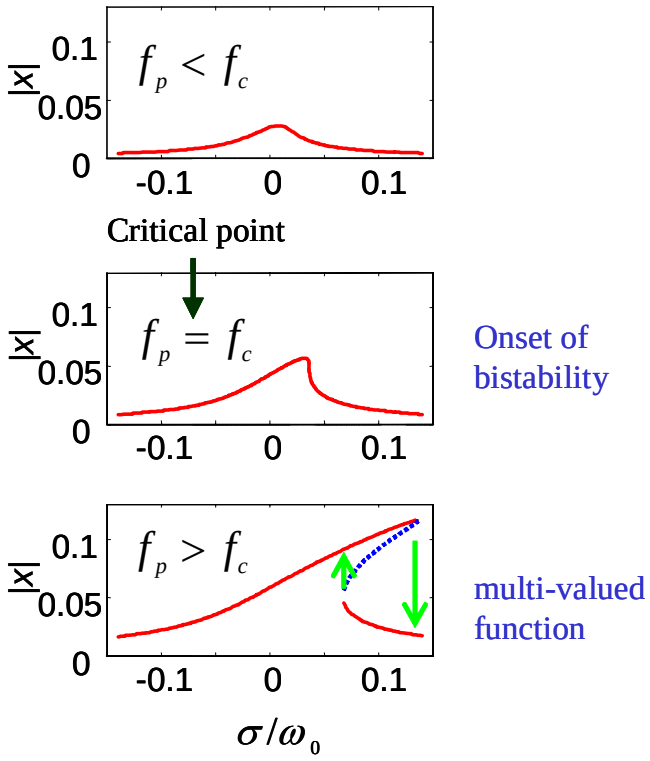

Figure 3.1: Frequency response for differenent valuse of pump force amplitude.

where the complex function $A(t)$ is a slowly varying function (relative to the time scale $1/\omega_p$). Thus, neglecting $\frac{d^2A}{dt^2}$, the expressions for $\dot{x}(t)$, $\ddot{x}(t)$ and $x^3(t)$ are given by:

$$\dot{x}(t) = \frac{1}{2}e^{i\omega_p t}(\dot{A} + i\omega_p A) + c.c, \tag{3.3a}$$

$$\ddot{x}(t) \approx \frac{1}{2}e^{i\omega_p t}(2i\omega_p \dot{A} - \omega_p^2 A) + c.c, \tag{3.3b}$$

$$x^3(t) = \left[\frac{1}{2}e^{i\omega_p t}A(t) + c.c\right]^3 = \frac{1}{8}e^{i3\omega_p t}A^3(t) + \frac{3}{8}A^2A^*e^{i\omega_p t} + c.c. \tag{3.3c}$$

Next, substituting expressions 3.3a-3.3c in the equation of motion (EOM) 3.1 gives

$$\frac{1}{2}e^{i\omega_p t}(2i\omega_p\dot{A}-\omega_p^2A)+2\mu\frac{1}{2}e^{i\omega_p t}(\dot{A}+i\omega_p A)+\omega_0^2(\frac{1}{2}e^{i\omega_p t}A(t)+\kappa\frac{3}{8}A^2A^*e^{i\omega_p t}) = \frac{1}{2}(f_p+f_se^{i(\delta t+\varphi)})e^{i\omega_p t}.$$

dividing both sides by $e^{i\omega_p t}$, one get for $\dot{A}$

$$\dot{A}(i\omega_p + \mu) = \frac{1}{2}(f_p + f_s e^{i(\delta t+\varphi)}) - \frac{1}{2}A(\omega_0^2 - \omega_p^2 + 2i\mu\omega_p) - \frac{3}{8}\kappa\omega_0^2A^2A^*. \tag{3.4}$$

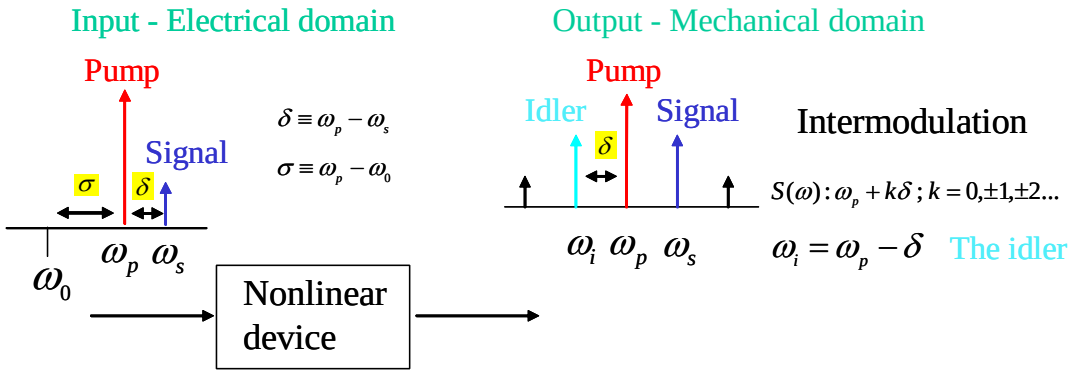

Figure 3.2: Frequency mixing in a nonlinear system.

For systems with high Q ($Q = \omega_0/2\mu \simeq 2000$), $\omega_p >> \mu$, hence the μ term in the left side of Eq. 3.4 can be neglected and to the first order $\omega_p \simeq \omega_0$ and $\omega_0^2 - \omega_p^2 \simeq -2\omega_0\sigma$. Finally the equation for the envelope function $A(t)$ is

$$\dot{A} = \frac{1}{2i\omega_0}(f_p + f_s e^{i(\delta t+\varphi)}) - A(i\sigma + \omega_0/2Q) + \frac{3}{8}i\kappa\omega_0 A^2 A^*. \tag{3.5}$$

$A(t)$ can be written as $A(t) = a_p + a_s e^{i\delta t} + a_i e^{-i\delta t}$, where the complex numbers a_p, a_s and a_i are the pump, signal and idler spectral components of $A(t)$ respectively and $|a_s|, |a_i| << |a_p|$. Keeping terms up to first order in a_s and a_i:

$$A^2A^* \simeq (a_p^2 + 2a_p a_s e^{j\delta t} + 2a_p a_i e^{-j\delta t})A^* \simeq a_p|a_p|^2 + 2|a_p|^2 a_s e^{j\delta t} + 2|a_p|^2 a_i e^{-j\delta t} + a_p^2 a_s^* e^{-j\delta t} + a_p^2 a_i^* e^{j\delta t}.$$

Grouping by exponential multipliers, one get three equations :

$$\frac{3}{8}\kappa\omega_0 a_p|a_p|^2 - \sigma a_p + j\mu a_p = \frac{1}{2}f_p/\omega_0 \qquad : e^0 \tag{3.6a}$$

$$\frac{3}{4}\kappa\omega_0|a_p|^2 a_s + \frac{3}{8}\kappa\omega_0 a_p^2 a_i^* - \delta a_s - \sigma a_s + j\mu a_s = \frac{1}{2}f_s e^{j\varphi}/\omega_0 \qquad : e^{j\delta t} \tag{3.6b}$$

$$\frac{3}{4}\kappa\omega_0|a_p|^2 a_i + \frac{3}{8}\kappa\omega_0 a_p^2 a_s^* - \delta a_i - \sigma a_i + j\mu a_i = 0 \qquad : e^{-j\delta t} \tag{3.6c}$$

Grouping by response amplitudes:

$$(\frac{3}{4}\kappa\omega_0|a_p|^2 - \sigma + j\mu) = \frac{1}{2a_p}f_p/\omega_0 + \frac{3}{8}\kappa\omega_0|a_p|^2 \tag{3.6d}$$

$$a_s(\frac{3}{4}\kappa\omega_0|a_p|^2 - \sigma + j\mu - \delta) + \frac{3}{8}\kappa\omega_0 a_p^2 a_i^* = \frac{1}{2}f_s e^{j\varphi}/\omega_0 \tag{3.6e}$$

$$a_i(\frac{3}{4}\kappa\omega_0|a_p|^2 - \sigma + j\mu - \delta) + \frac{3}{8}\kappa\omega_0 a_p^2 a_s^* = 0 \tag{3.6f}$$

Eq. 3.6a can be identified as Duffing equation when the only excitation is the pump. Taking the absolute values from both sides of Eq. 3.6a gives:

$$\frac{9}{64}\kappa^2\omega_0^2|a_p|^6 - \frac{3}{4}\sigma\kappa\omega_0|a_p|^4 + (\sigma^2+\mu^2)|a_p|^2 = \frac{1}{4}f_p^2/\omega_0^2 \tag{3.7}$$

3.2 Special Points

Points of special interest:

$$\text{Jump points: } \frac{\partial|a_p|}{\partial\sigma} = -\infty \ (\frac{\partial\sigma}{\partial|a_p|} = 0) \tag{3.8a}$$

$$\text{Critical point: 3.8a and } \frac{\partial^2\sigma}{\partial|a_p|^2} = 0 \tag{3.8b}$$

The critical point is a combination of σ and a_p where the resonance curve has an infinite slope and the system is on edge of hysteresis (multiple stable solutions).

For the ease of the expressions let $\alpha \equiv \kappa\omega_0$. Differentiating 3.7 twice with respect to $|a_p|$:

$$2\sigma\frac{\partial\sigma}{\partial|a_p|}|a_p| + 2\sigma^2 - \frac{3}{4}\alpha|a_p|^3\frac{\partial\sigma}{\partial|a_p|} - 3\alpha|a_p|^2\sigma + \frac{27}{32}\alpha^2|a_p|^4 + 2\mu^2 = 0 : \frac{\partial}{\partial|a_p|} \tag{3.9}$$

$$2(\frac{\partial\sigma}{\partial|a_p|})^2|a_p| + 2\sigma\frac{\partial^2\sigma}{\partial|a_p|^2}|a_p| + 2\sigma\frac{\partial\sigma}{\partial|a_p|} + 4\sigma\frac{\partial\sigma}{\partial|a_p|} - \frac{9}{4}\alpha|a_p|^2 \ \ ... : \frac{\partial^2}{\partial|a_p|^2} \tag{3.10}$$

$$... - \frac{3}{4}\alpha|a_p|^3\frac{\partial^2\sigma}{\partial|a_p|^2} - 6\alpha|a_p|\sigma - 3\alpha|a_p|^2\frac{\partial\sigma}{\partial|a_p|} + \frac{27}{8}\alpha^2|a_p|^3 = 0$$

isolating $\frac{\partial\sigma}{\partial|a_p|}$and $\frac{\partial^2\sigma}{\partial|a_p|^2}$

$$\frac{\partial\sigma}{\partial|a_p|} = \frac{\frac{27}{32}\alpha^2|a_p|^4 - 3\alpha|a_p|^2\sigma + 2(\sigma^2+\mu^2)}{\frac{3}{4}\alpha|a_p|^3 - 2\sigma|a_p|} \tag{3.11a}$$

$$\frac{\partial^2\sigma}{\partial|a_p|^2} = \frac{\frac{\partial\sigma}{\partial|a_p|}(2(\frac{\partial\sigma}{\partial|a_p|})|a_p| + 6\sigma - \frac{21}{4}\alpha|a_p|^2) - 6\alpha|a_p|\sigma + \frac{27}{8}\alpha^2|a_p|^3}{\frac{3}{4}\alpha|a_p|^3 - 2\sigma|a_p|} \tag{3.11b}$$

and applying 3.8:

$$\frac{27}{32}\alpha^2|a_p|^4 - 3\alpha|a_p|^2\sigma + 2(\sigma^2+\mu^2) = 0 \qquad \text{Jump points} \tag{3.12a}$$

$$|a_{p_c}|^2 = \frac{16}{9\alpha}\sigma \qquad \text{Critical point} \tag{3.12b}$$

Substituting 3.12b into 3.12a, we get the values of σ and a_p in the critical point

$$\begin{aligned} \sigma_c &= \sqrt{3}\mu = \sqrt{3}\omega_0/2Q \\ |a_{p_c}|^2 &= \frac{16}{3\sqrt{3}}\frac{\mu}{\alpha} = \frac{8}{3\sqrt{3}\kappa Q} \end{aligned} \tag{3.13}$$

Substituting 3.13 in 3.7 gives the critical force amplitude f_c

$$\begin{aligned} \frac{64}{81\alpha}\sigma^3 - \frac{3\times 64}{81\alpha}\sigma^3 + \frac{9\times 16}{81\alpha}\sigma^3 + \frac{16}{9\alpha}\mu^2\sigma &= \frac{1}{4}f_c^2/\omega_0^2 \\ \Longrightarrow \sigma^3 + 9\mu^2\sigma = 4\sigma^3 &= \frac{81}{64}\alpha f_c^2/\omega_0^2 \\ \Longrightarrow f_c/\omega_0 &= \frac{16}{3\sqrt[4]{3}}\mu\sqrt{\frac{\mu}{\alpha}} = \frac{8\omega_0}{3\sqrt[4]{3}Q}\sqrt{\frac{1}{2\kappa Q}} \end{aligned} \tag{3.14}$$

3.3 Solutions for Signal and Idler

manipulation of 3.6e and 3.6f gives

$$a_s = \frac{\frac{1}{2}(f_s/\omega_0)e^{j\varphi} - \frac{3}{8}\kappa\omega_0 a_p^2 a_i^*}{\frac{3}{4}\kappa\omega_0|a_p|^2 - \delta - \sigma + j\frac{\omega_0}{2Q}} \tag{3.15a}$$

$$a_i = \frac{-\frac{3}{8}\kappa\omega_0 a_p^2 a_s^*}{\frac{3}{4}\kappa\omega_0|a_p|^2 - \delta - \sigma + j\frac{\omega_0}{2Q}} \tag{3.15b}$$

Taking complex conjugative of 3.15b

$$a_i^* = \frac{-\frac{3}{8}\kappa\omega_0 (a_p^*)^2 a_s}{\frac{3}{4}\kappa\omega_0|a_p|^2 - \delta - \sigma - j\frac{\omega_0}{2Q}} \tag{3.16}$$

and substituting it into 3.15a:

$$a_s = \frac{\frac{1}{2}(f_s/\omega_0)e^{j\varphi} + \frac{(\frac{3}{8}\kappa\omega_0|a_p|^2)^2 a_s}{\frac{3}{4}\kappa\omega_0|a_p|^2 - \delta - \sigma - j\frac{\omega_0}{2Q}}}{\frac{3}{4}\kappa\omega_0|a_p|^2 - \delta - \sigma + j\frac{\omega_0}{2Q}}$$

$$a_s(1 - \frac{(\frac{3}{8}\kappa\omega_0|a_p|^2)^2}{|\frac{3}{4}\kappa\omega_0|a_p|^2 - \delta - \sigma + j\frac{\omega_0}{2Q}|^2}) = \frac{\frac{1}{2}(f_s/\omega_0)e^{j\varphi}}{\frac{3}{4}\kappa\omega_0|a_p|^2 - \delta - \sigma + j\frac{\omega_0}{2Q}}$$

Final solution for signal and idler amplitudes as functions of pump amplitude:

$$a_s = \frac{\frac{1}{2}(f_s/\omega_0)e^{j\varphi} \times (\frac{3}{4}\kappa\omega_0|a_p|^2 - \delta - \sigma - j\frac{\omega_0}{2Q})}{|\frac{3}{4}\kappa\omega_0|a_p|^2 - \delta - \sigma + j\frac{\omega_0}{2Q}|^2 - (\frac{3}{8}\kappa\omega_0|a_p|^2)^2} \tag{3.17a}$$

$$a_i = \frac{-\frac{1}{2}(f_s/\omega_0)e^{-j\varphi} \times \frac{3}{8}\kappa\omega_0 a_p^2}{|\frac{3}{4}\kappa\omega_0|a_p|^2 - \delta - \sigma + j\frac{\omega_0}{2Q}|^2 - (\frac{3}{8}\kappa\omega_0|a_p|^2)^2} \tag{3.17b}$$

Now we would like to check the behavior of 3.17 near the critical point. We assume $\delta \ll \sigma$ (signal frequency very close to pump frequency) and use the expressions for the critical point (3.13). In this case we get divergence of a_s and a_i in the critical point

$$|a_{s_c}| \approx |a_{i_c}| \approx \frac{f_s}{2\omega_0\delta} \overset{\delta\to 0}{\to} \infty \tag{3.18}$$

Thus, in our model which assumes that $|a_s|$ and $|a_i|$ are small, and takes nonlinearity into account to lowest order only, the amplification diverges in the bifurcation point in the limit $\delta \to 0$. When $|a_s|$ and $|a_i|$ become comparable with $|a_p|$, however, the former assumptions are no longer valid and higher order terms have to be taken into account.

3.4 Calculation of a_p, a_s and a_i

The pump, signal, and idler responses a_p, a_s and a_i were calculated using a matlab program [43] and are shown in Fig. 3.3. As can be shown, For a small (sub-critical) f_p, the signal response is nearly Lorentzian, while for $f_p = f_c$ and $f_p > f_c$, both signal and idler response diverge in the vicinity of the jump points of the pump response. When the pump is tuned to the edge of the bistability region, the resonator is very sensitive to fluctuations.

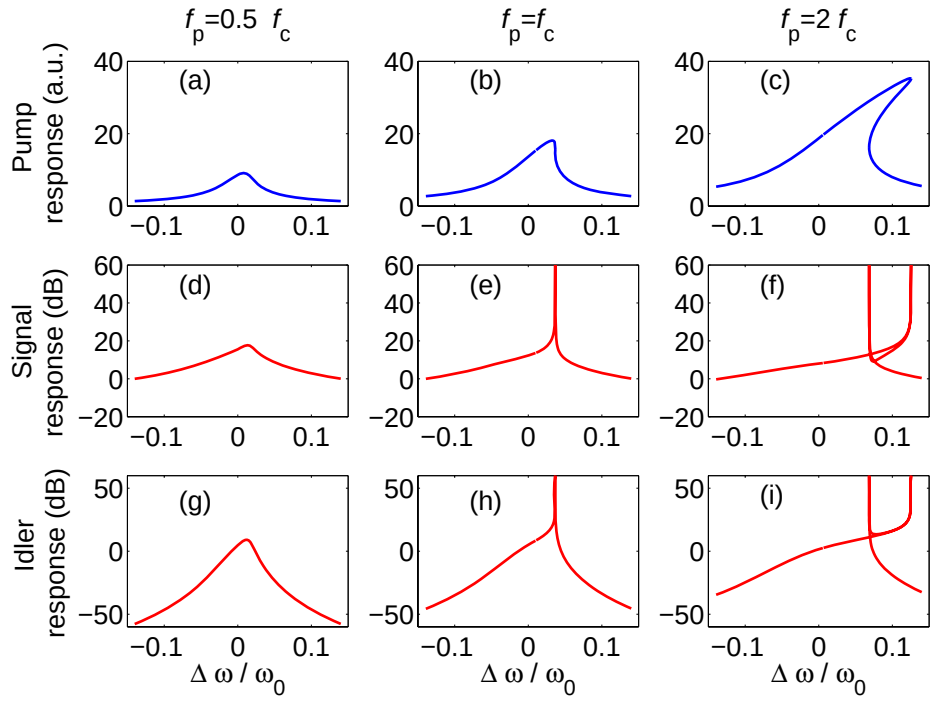

Figure 3.3: Calculation of the pump, signal, and idler responses ($|a_p|$, $|a_s|$, $|a_i|$) for vanishing offset frequency δ, shown for sub-critical case $f_p = 0.5 f_c$ (a,d,g), critical case $f_p = f_c$ (b,e,h), and over-critical case $f_p = 2 f_c$ (c,f,i). The y-axis of the pump is shown in a linear scale while the signal's and idler's response are normalized to the signal's excitation amplitude and are shown in a logarithmic scale. The signal's and idler's response diverge at the critical point and at the jump points. The parameters for this example are $\kappa = 10^{-4}\,\mathrm{m}^{-2}$, $\mu = 10^2\,\mathrm{Hz}$, $\omega_0/2\pi = 1\,\mathrm{MHz}$, and $\delta/2\pi = 10\,\mathrm{Hz}$.

3.5 Homodyne Detection

Because of intermodulation gain, a parametric amplifier can establish correlations [69] between the output at $\omega_p + \delta$ (signal) and $\omega_p - \delta$ (idler). When delivered to a mixer whose local oscillator is phase-locked to the pump, these correlations can result in noise fluctuations reduced below that which the mixer would see if the signal delivered to the parametric amplifier were, instead, directly delivered to the mixer. This noise reduction is called squeezing, and it can occur with either thermal or quantum noise [70].

We now assume that the detector's signal is downconverted by mixing with a local oscillator (LO) that is tuned to the pump frequency ω_p and has a controlled phase $\phi_{\rm LO}$ (see Fig. 3.4). Suppose that the LO voltage is given by $V^{\rm LO}(t) = V_0^{\rm LO}\cos(\omega_p t + \phi_{\rm LO})$ and the mixer's output is given by $V_{\rm MO} = Mx(t)V^{\rm LO}(t)$ where M is a constant term depending on the optical detector's sensitivity, amplification and the mixing factor. After passing through a low pass filter (LPF), the output signal is

$$\frac{1}{4}MV_0^{\rm LO}[A(t)e^{-i\phi_{\rm LO}} + c.c.] \ .$$

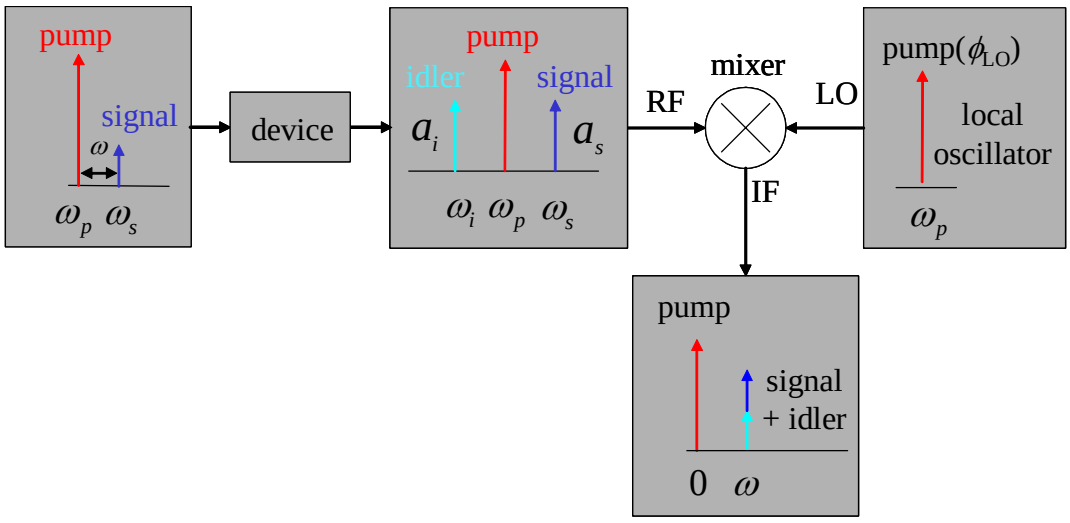

Figure 3.4: Homodyne detection scheme

The interesting measured quantity is the amplitude $R(\delta)$ of the spectral component of the output signal at frequency δ. $R(\delta)$ depends on the LO phase ϕ_{LO} and is given by

$$R(\delta) = \frac{1}{2}MV_0^{\rm LO}\left|a_s e^{-i\phi_{\rm LO}} + a_i^* e^{i\phi_{\rm LO}}\right| \ . \tag{3.19}$$

The spectral component a_s and a_i are added phasorically, and so they can add constructively or destructively depending on the LO phase. $R(\delta)$ is proportional to the amplitude of this phasors sum. As ϕ_{LO} is varied, the term $\left|a_s e^{-i\phi_{\mathrm{LO}}} + a_i^* e^{i\phi_{\mathrm{LO}}}\right|$ oscillates between the minimum value $||a_s| - |a_i||$ and the maximum one $|a_s| + |a_i|$. When $\delta \to 0$, and a_p is tuned to the bifurcation point, we have $|a_s| \simeq |a_i| \simeq f_s/2\omega_0\delta$ (Eq. 3.18), hence $R(\delta)_{\max} = MV_0^{LO} f_s/2\omega_0\delta$ and $R(\delta)_{\min}/R(\delta)_{\max} \to 0$.

3.6 Response to Injected Noise

To study the response to an injected noise, the resonator is excited by a fixed pump near the bifurcation point, together with white noise. In this case Eq. 3.1 is a Langevin equation with $F(t) = f_p \cos(\omega_p t) + F_n(t)$ where $F_{\rm n}(t)$ is a white noise having a vanishing mean $\langle F_{\rm n}(t) \rangle = 0$, and spectral density $S_{F_n} = 4\omega_0 k_B T_{\rm eq}/m_{eff}Q$ [19]. Here $T_{\rm eq}$ is the equivalent temperature of the applied voltage noise and m_{eff} is the effective mass of the fundamental mode. In this case, the displacement spectral density measured at the mixer's output will consist of two contributions, namely, the pump response (δ-function peaked at $\delta = 0$), and a continuous part $S_x(\delta)$ due to noise. The limit S_x of $S_x(\delta)$ when $\delta \to 0$, was calculated in Ref. [71] and is given by

$$S_x = \frac{1 + 2\zeta \cos(\phi_{\rm LO} - \phi_0) + \zeta^2}{(1-\zeta^2)^2} S_{x0}, \tag{3.20}$$

where

$$S_{x0} = S_{F_n} / \left\{ 4\omega_0^2 \left[\mu^2 + \left(\omega_p - \omega_0 - \frac{3}{2}\omega_0 \kappa \left| a_p \right|^2 \right)^2 \right] \right\}$$

and ϕ_0 and ζ are real parameters. The derivation of the above expressions using Hamilton equations of motion is the subject of section 3.8. While ζ vanishes in the linear region, its largest value $\zeta = 1$ is obtained along the edge of the bistability region. Eq. (3.20) implies that when $\delta \to 0$, the output noise will oscillate between a maximum value, corresponding to the amplified quadrature, and a minimum one, corresponding to the deamplified (or squeezed) quadrature, as $\phi_{\rm LO}$ is varied.

$$\begin{aligned} [S_x]_{\max} &= \frac{S_{x0}}{(1-\zeta)^2} \\ [S_x]_{\min} &= \frac{S_{x0}}{(1+\zeta)^2}. \end{aligned} \tag{3.21}$$

Thus, the largest amplification obtained by this model diverges at the bifurcation point, whereas noise squeezing is limited to a factor of 4.

3.7 Test of Nonlinear Dissipation

Taking nonlinear dissipation into account, the equation of motion is given by

$$\ddot{x} + 2\mu(1 + \beta x^2)\dot{x} + \omega_0^2(1 + \kappa x^2)x = F(t), \tag{3.22}$$

where μ and β are the linear and nonlinear damping constants respectively.

The relative importance of nonlinear damping can be characterized by the dimensionless parameter $p = 2\sqrt{3}\mu\beta/\kappa\omega_0$ [36].

In this case, the detuning in the critical point is given by

$$\sigma_c = \frac{\mu}{\sqrt{3}}\frac{p+3}{1-p}.$$

The relatively low value of $p \simeq 0.05$, obtained from the measured values of ω_0, μ and the detuning of the critical point, indicates that the effect of nonlinear damping in our device is relatively weak and will be neglected in the rest of this work.

A detailed investigation of nonlinear dissipation is presented in appendix1.

3.8 Stochastic solution using the Hamilton formalism

We now solve the EOM using the Hamilton formalism in the general case [43],[71]. This is very useful due to the fact that similar equations describe other types of resonators, e.g. RF or optical resonators where the resonators are excited by an incoming wave.

3.8.1 Hamiltonian

Consider a nonlinear mechanical resonator of mass m, resonance frequency ω_0, damping rate γ, cubic nonlinear constant K, and nonlinear damping rate γ_3. The parameters γ, K, and γ_3 are related but don't equal to the parameters from the previous sections as they are used in the Hamilton formalism as coupling parameters. The relationship between the parameters is given by

$$\mu = \gamma; \quad \beta = \frac{\gamma_3}{3\gamma x_0^2}; \quad \kappa = \frac{2K}{3\omega_0 x_0^2}$$

The resonator is driven by harmonic pump force at frequency ω_p. The complex amplitude of the force f is written as

$$f = -2im\omega_p x_0 p^{1/2} e^{i\phi_p} \ , \tag{3.23}$$

where p is positive real, ϕ_p is real, and x_0 is given by

$$x_0 = \sqrt{\frac{\hbar}{2m\omega_0}} \ . \tag{3.24}$$

The Hamiltonian of the system is given by [43]

$$H = H_1 + H_{a_2} + H_{a_3} + H_{c2} + H_{c3} \ , \tag{3.25}$$

where H_1 is the Hamiltonian of the driven nonlinear resonator

$$\begin{aligned} H_1 = {} & \hbar\omega_0 A^\dagger A + \frac{\hbar}{2} K A^\dagger A^\dagger A A \\ & + \hbar p^{1/2} \left(i e^{i\left(\phi_p - \omega_p t\right)} A^\dagger - i e^{-i\left(\phi_p - \omega_p t\right)} A \right) \ . \end{aligned} \tag{3.26}$$

The resonator's creation and annihilation operators satisfy the following commutation relation

$$\left[A, A^\dagger\right] = AA^\dagger - A^\dagger A = 1 \ . \tag{3.27}$$

The operator a_2 serves as a linear loss port (bath) and the operator a_3 serves as the two-photon loss port (bath). The Hamiltonians H_{a2} and H_{a3} associated with both baths are given by

$$H_{a2} = \int \mathrm{d}\omega \hbar\omega a_2^\dagger(\omega)\, a_2(\omega) \ , \tag{3.28}$$

$$H_{a3} = \int \mathrm{d}\omega \hbar\omega a_3^\dagger(\omega)\, a_3(\omega) \ . \tag{3.29}$$

The major contribution to the interaction between the resonator mode and the modes in the baths arises from those modes whose frequencies are in the resonance bandwidth of the driven mode. Assuming that the coupling constants, which characterizes the interaction between the resonator mode and the modes in the baths, remain essentially constant in this narrow frequency range allows expressing the coupling Hamiltonians using frequency independent coupling constants. The Hamiltonian

H_{c2} linearly couples the bath modes $a_2(\omega)$ to the resonator mode A

$$H_{c2} = \hbar\sqrt{\frac{\gamma}{\pi}}\int \mathrm{d}\omega \left[A^\dagger a_2(\omega) + a_2^\dagger(\omega) A\right] \ , \tag{3.30}$$

whereas H_{c3} describes two-phonon absorptive coupling of the resonator mode to the bath modes $a_3(\omega)$ in which two resonator phonons are destroyed for every bath phonon created

$$H_{c3} = \hbar\sqrt{\frac{\gamma_3}{\pi}}\int \mathrm{d}\omega \left[A^\dagger A^\dagger a_3(\omega) + a_3^\dagger(\omega) A A\right] \ . \tag{3.31}$$

The bath modes are boson modes, satisfying the usual Bose commutation relations

$$[a_n(\omega), a_n^\dagger(\omega')] = \delta(\omega - \omega') \ , \tag{3.32}$$

$$[a_n(\omega), a_n(\omega')] = 0 \ . \tag{3.33}$$

3.8.2 Equations of Motion

We now generate the Heisenberg equations of motion according to

$$i\hbar\frac{dO}{dt} = [O, H] \ , \tag{3.34}$$

where O is an operator and H is the total Hamiltonian

$$\begin{aligned} i\frac{\mathrm{d}A}{\mathrm{d}t} &= \omega_0 A + K A^\dagger A A + i p^{1/2} e^{i\phi_p} e^{-i\omega_p t} \\ &\quad + \sqrt{\frac{\gamma}{\pi}}\int \mathrm{d}\omega a_2(\omega) + 2\sqrt{\frac{\gamma_3}{\pi}} A^\dagger \int \mathrm{d}\omega a_3(\omega) \ , \end{aligned} \tag{3.35}$$

$$\frac{\mathrm{d}a_2(\omega)}{\mathrm{d}t} = -i\omega a_2(\omega) - i\sqrt{\frac{\gamma}{\pi}} A \ , \tag{3.36}$$

$$\frac{\mathrm{d}a_3(\omega)}{\mathrm{d}t} = -i\omega a_3(\omega) - i\sqrt{\frac{\gamma_3}{2\pi}} A A \ . \tag{3.37}$$

Using the standard method of Gardiner and Collett [72], and employing a transformation to a reference frame rotating at angular frequency ω_p

$$A = C e^{-i\omega_p t} \ , \tag{3.38}$$

yield the following equation for the operator C

$$\frac{\mathrm{d}C}{\mathrm{d}t} + \Theta = F\left(t\right) \ , \tag{3.39}$$

where

$$\Theta = \left[\gamma + i\left(\omega_0 - \omega_p\right) + \left(iK + \gamma_3\right) C^{\dagger} C\right] C - p^{1/2} e^{i\phi_p} \ . \tag{3.40}$$

The noise term $F\left(t\right)$ is given by

$$F = -i\sqrt{2\gamma} a_2^{in} e^{i\omega_p t} - i2\sqrt{\gamma_3} C^{\dagger} a_3^{in} e^{2i\omega_p t} \ , \tag{3.41}$$

where

$$a_2^{in}\left(t\right) = \frac{1}{\sqrt{2\pi}} \int \mathrm{d}\omega e^{-i\omega\left(t-t_0\right)} a_2\left(t_0, \omega\right) \ , \tag{3.42}$$

$$a_3^{in}\left(t\right) = \frac{1}{\sqrt{2\pi}} \int \mathrm{d}\omega e^{-i\omega\left(t-t_0\right)} a_3\left(t_0, \omega\right) \ . \tag{3.43}$$

In the noiseless case, namely when $F = 0$, the equation of motion for the displacement x of the vibrating mode can be written as

$$\begin{aligned} &\frac{\mathrm{d}^2 x}{\mathrm{d}t^2} + 2\gamma \left[1 + \frac{\gamma_3}{3\gamma}\left(\frac{x}{x_0}\right)^2\right] \frac{\mathrm{d}x}{\mathrm{d}t} + \omega_0^2 \left[1 + \frac{2K}{3\omega_0}\left(\frac{x}{x_0}\right)^2\right] x \\ &= \frac{f}{m} e^{-i\omega_p t} + c.c. \ . \end{aligned} \tag{3.44}$$

Note, however, that Eq. (3.44) does not result directly from Eq. (3.39) in the case $F = 0$, but rather it is an equation of motion for x, which leads to Eq. (3.39) when a slowly varying approximation is employed as we did in the previous sections.

3.8.3 Linearization

Let $C = C_m + c$, where C_m is a complex number for which

$$\Theta\left(C_m, C_m^*\right) = 0 \ , \tag{3.45}$$

namely, C_m is a steady state solution of Eq. (3.39) for the noiseless case $F = 0$. When the noise term F can be considered as small, one can find an equation of motion for

the fluctuation around C_m by linearizing Eq. (3.39)

$$\frac{\mathrm{d}c}{\mathrm{d}t} + Wc + Vc^\dagger = F \ , \tag{3.46}$$

where

$$W = \left.\frac{\partial \Theta}{\partial C}\right|_{C=C_m} = \gamma + i\left(\omega_0 - \omega_p\right) + 2\left(iK + \gamma_3\right) C_m^* C_m \ , \tag{3.47}$$

and

$$V = \left.\frac{\partial \Theta}{\partial C^\dagger}\right|_{C=C_m} = \left(iK + \gamma_3\right) C_m^2 \ . \tag{3.48}$$

Mean-Field Solution

Using the notation

$$C_m = E^{1/2} e^{i\phi_m} \ , \tag{3.49}$$

where E is positive and ϕ_m is real, Eq. (3.45) reads

$$\left[\gamma + i\left(\omega_0 - \omega_p\right) + \left(iK + \gamma_3\right) E\right] E^{1/2} e^{i\phi_m} = p^{1/2} e^{i\phi_p} \ . \tag{3.50}$$

Multiplying each side by its complex conjugate yields

$$\left[\left(\gamma + \gamma_3 E\right)^2 + \left(\omega_0 - \omega_p + KE\right)^2\right] E = p \ . \tag{3.51}$$

Finding E by solving the cubic polynomial Eq. (3.51) allows calculating C_m using Eq. (3.50).

Taking the derivative of Eq. (3.51) with respect to the drive frequency ω_p, one finds

$$\frac{\partial E}{\partial \omega_p} = \frac{2(\omega_0 - \omega_p + KE)E}{|W|^2\left(1 - \zeta^2\right)} \ , \tag{3.52}$$

where

$$\zeta = \left|\frac{V}{W}\right| \ . \tag{3.53}$$

Similarly for the drive amplitude p

$$\frac{\partial E}{\partial p} = \frac{1}{|W|^2\left(1 - \zeta^2\right)} \ . \tag{3.54}$$

Note that, as shown below, the value $\zeta = 1$ occurs along the edge of the bistability region.

The bifurcation point

At the bifurcation (cusp) point, namely at the onset of bistability, the following holds

$$\frac{\partial \omega_p}{\partial E} = \frac{\partial^2 \omega_p}{\partial E^2} = 0 \ . \tag{3.55}$$

Such a point occurs only if the nonlinear damping is sufficiently small [43], namely, only when the following condition holds

$$|K| > \sqrt{3}\gamma_3 \ . \tag{3.56}$$

At the bifurcation point the drive frequency and amplitude are given by

$$\left(\omega_p - \omega_0\right)_c = \gamma \frac{K}{|K|} \left[\frac{4\gamma_3 |K| + \sqrt{3}\left(K^2 + \gamma_3^2\right)}{K^2 - 3\gamma_3^2} \right] \ , \tag{3.57}$$

$$p_c = \frac{8}{3\sqrt{3}} \frac{\gamma^3 (K^2 + \gamma_3^2)}{\left(|K| - \sqrt{3}\gamma_3\right)^3} \ , \tag{3.58}$$

and the resonator mode amplitude is

$$E_c = \frac{2\gamma}{\sqrt{3}\left(|K| - \sqrt{3}\gamma_3\right)} \ . \tag{3.59}$$

3.8.4 Basins of Attraction

In the bistable region Eq. (3.45) has 3 different solutions, labeled as C_1, C_2 and C_3, where both stable solutions C_1 and C_3 are attractors, and the unstable solution C_2 is a saddle point. The bistable region Λ in the plane of parameters (ω_p, p) is seen in the colormap in Fig. 3.5. The lines that constitute the edge of the bistability region are usually called bifurcation lines. The cubic nonlinear constant in this example is $K/\omega_0 = 0.001$, and the damping constants are $\gamma/\omega_0 = 0.02$, $\gamma_3 = 0.1K/\sqrt{3}$. The color in the bistable region Λ indicates the difference $|C_3|^2 - |C_1|^2$. The bifurcation point at $\omega_p - \omega_0 = \left(\omega_p - \omega_0\right)_c$ and $p = p_c$ is labeled as B_c in the figure.

Figure 3.6 (a) shows some flow lines obtained by integrating Eq. (3.39) numerically for the noiseless case $F = 0$. The red and blue lines represent flow toward

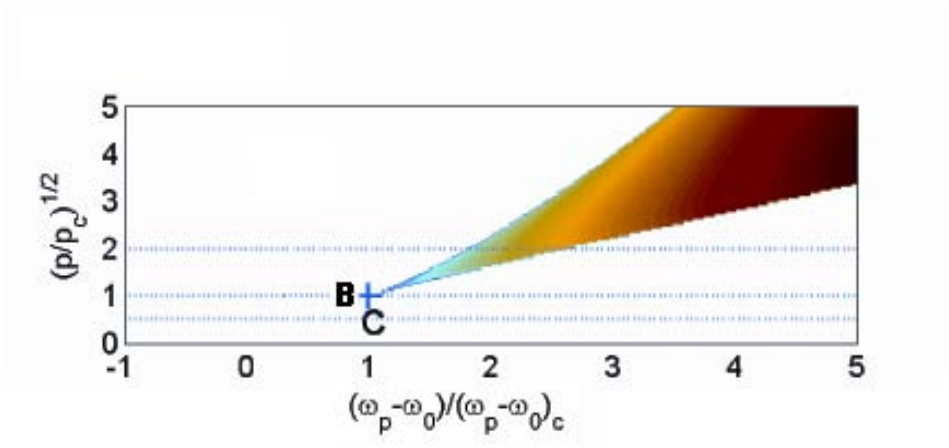

Figure 3.5: The bistable region Λ in the (ω_p, p) plane. The color in the bistable region indicates the difference $|C_3|^2 - |C_1|^2$. The blue lines cross the curves at the sub-critical, critical, and over-critical driving force respectively. The Bifurcation point is markd by B_c.

the attractors at C_1 and C_3 respectively. The green line is the seperatrix, namely the boundary between the basins of attraction of the attractors at C_1 and C_3. A closer view of the region near C_1 and C_2 is given in Fig. 3.6 (b). This figure shows also, an example of a random motion near the attractor at C_1 (seen as a cyan line). The line was obtained by numerically integrating Eq. (3.39) with a non vanishing fluctuating force F. The random walk demonstrates noise squeezing (to be further discussed below), where the fluctuations obtain their largest and smallest values along the directions of the local principle axes (see the last subsection).

The solution of the equation of motion (3.46) was found in Ref. [43]

$$c(t) = \int_{-\infty}^{\infty} \mathrm{d}t' G(t-t') \Gamma(t') \ , \tag{3.60}$$

where

$$\Gamma(t) = \frac{\mathrm{d}F(t)}{dt} + W^* F(t) - V F^{\dagger}(t) \ . \tag{3.61}$$

The propagator is given by

$$G(t) = u(t) \frac{e^{-\lambda_0 t} - e^{\lambda_1 t}}{\lambda_1 - \lambda_0} \ , \tag{3.62}$$

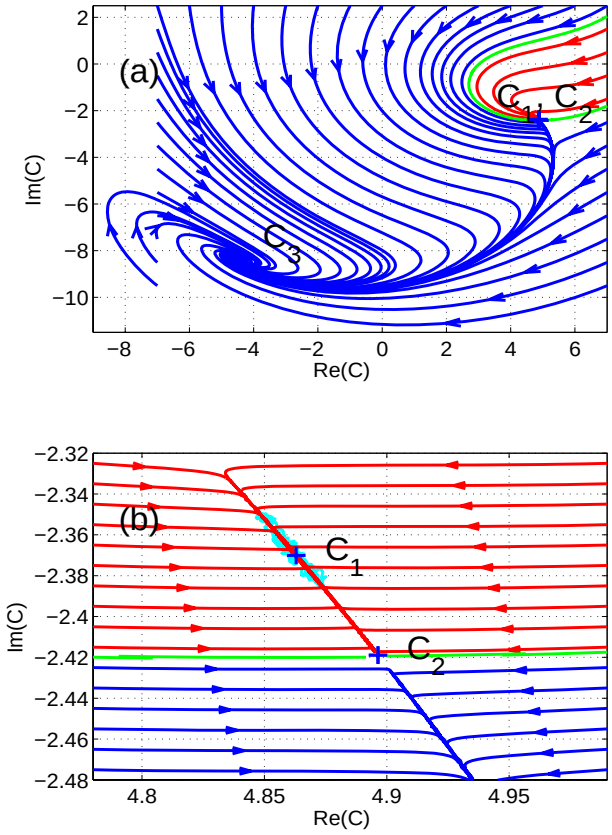

Figure 3.6: Flow lines obtained by integrating Eq. (3.39) for the noiseless case $F = 0$. The points C_1 and C_3 are attractors, and C_2 is a saddle point. The green line is the seperatrix, namely the boundary between the basins of attraction of both attractors. Panel (a) shows a wide view, whereas panel (b) shows a closer view of the region near C_1 and C_2. The cyan line near the attractor C_1 in panel (b) demonstrates random motion in the presence of noise.

where $u(t)$ is the unit step function

$$u(t) = \begin{cases} 1, & t > 0 \\ 1/2, & t = 0 \\ 0, & t < 0 \end{cases} , \tag{3.63}$$

and λ_0 and λ_1 are the eigenvalues of the homogeneous equation, which satisfy

$$\lambda_0 + \lambda_1 = 2W' , \tag{3.64}$$

$$\lambda_0 \lambda_1 = |W|^2 - |V|^2 , \tag{3.65}$$

where W' is the real part of W. Thus one has

$$\lambda_{0,1} = W' \left(1 \pm \sqrt{1 + \frac{|W|^2}{(W')^2} \left(\zeta^2 - 1 \right)} \right) \ , \tag{3.66}$$

or

$$\lambda_{0,1} = \gamma + 2\gamma_3 E \pm \sqrt{\left(K^2 + \gamma_3^2 \right) E^2 - \left(\omega_0 - \omega_p + 2KE \right)^2} \ . \tag{3.67}$$

3.8.5 Homodyne Detection

Consider the case where homodyne detection is employed for readout. In this case the output signal of a displacement detector monitoring the mechanical motion is mixed with a local oscillator at the same frequency as the frequency of the pump ω_p and having an adjustable phase $\phi_{\rm LO}$ ($\phi_{\rm LO}$ is real). The local oscillator is assumed to be noiseless. The output signal of the homodyne detector is proportional to

$$X_{\phi_{\rm LO}}(t) = e^{i\phi_{\rm LO}} C(t) + e^{-i\phi_{\rm LO}} C^\dagger(t) \ . \tag{3.68}$$

The time varying signal $X_{\phi_{\rm LO}}(t)$ can be characterized by its average

$$X_0 = \left\langle X_{\phi_{\rm LO}}(t) \right\rangle \ , \tag{3.69}$$

and by its time auto-correlation function

$$K(t'-t) = \left\langle \left[X_{\phi_{\rm LO}}(t) - X_0 \right] \left[X_{\phi_{\rm LO}}(t') - X_0 \right] \right\rangle \ . \tag{3.70}$$

The correlation function is expected to be an even function of $t'-t$ with a maximum at $t'-t=0$. The correlation time characterizes the width of that peak. Consider a measurement in which $X_{\phi_{\rm LO}}(t)$ is continuously monitored in the time interval $[0,\tau]$. Let X_τ be an estimator of the average value of $X_{\phi_{\rm LO}}(t)$

$$X_\tau = \frac{1}{\tau} \int_0^\tau {\rm d}t \ X_{\phi_{\rm LO}}(t) \ . \tag{3.71}$$

Clearly X_τ is unbiased, and its variance is given by

$$\left\langle (X_\tau - X_0)^2 \right\rangle = \frac{1}{\tau^2} \int_0^\tau {\rm d}t \int_0^\tau {\rm d}t' \ K(t'-t) \ . \tag{3.72}$$

Assuming the case where the measurement time τ is much longer than the correlation time. For this case one can employ the approximation

$$\left\langle (X_\tau - X_0)^2 \right\rangle = \frac{1}{\tau} \int_{-\infty}^{\infty} \mathrm{d}t \; K(t) \;\; , \tag{3.73}$$

or in terms of the spectral density $P_{\phi_{\mathrm{LO}}}(\omega)$ of $X_{\phi_{\mathrm{LO}}}(t)$

$$\left\langle (X_\tau - X_0)^2 \right\rangle = \frac{2\pi}{\tau} P_{\phi_{\mathrm{LO}}}(0) \;\; . \tag{3.74}$$

3.8.6 Spectral Density

To calculate the spectral density $P_{\phi_{\mathrm{LO}}}(\omega)$ of $X_{\phi_{\mathrm{LO}}}(t)$ it is convenient to introduce the Fourier transform

$$c(t) = \frac{1}{\sqrt{2\pi}} \int_{-\infty}^{\infty} \mathrm{d}\omega c(\omega) \, e^{-i\omega t} \;\; , \tag{3.75}$$

$$\Gamma(t) = \frac{1}{\sqrt{2\pi}} \int_{-\infty}^{\infty} \mathrm{d}\omega \Gamma(\omega) \, e^{-i\omega t} \;\; . \tag{3.76}$$

Assuming the bath modes are in thermal equilibrium, one finds

$$\langle F(\tau) \rangle = \left\langle F^\dagger(\tau) \right\rangle = 0 \;\; , \tag{3.77}$$

$$\langle F(\tau) F(\tau') \rangle = \left\langle F^\dagger(\tau) F^\dagger(\tau') \right\rangle = 0 \;\; , \tag{3.78}$$

$$\left\langle F(\tau) F^\dagger(\tau') \right\rangle = (\lambda_0 + \lambda_1) \, \delta(\tau - \tau') \, \langle n_{\omega_0} \rangle \;\; , \tag{3.79}$$

$$\left\langle F^\dagger(\tau) F(\tau') \right\rangle = (\lambda_0 + \lambda_1) \, \delta(\tau - \tau') \, (\langle n_{\omega_0} \rangle + 1) \;\; . \tag{3.80}$$

where

$$\langle n_\omega \rangle = \frac{1}{e^{\beta\hbar\omega} - 1} \;\; , \tag{3.81}$$

and $\beta = 1/k_B T$.

In Ref. [43], [73], we have found that the following holds

$$c(\omega) = \frac{\Gamma(\omega)}{(-i\omega + \lambda_0)(-i\omega + \lambda_1)} \;\; . \tag{3.82}$$

where

$$\langle \Gamma(\omega) \rangle = \left\langle \Gamma^\dagger(\omega) \right\rangle = 0 \;\; , \tag{3.83}$$

$$\langle \Gamma(\omega') \Gamma(\omega) \rangle = \mathcal{N}_1(\omega) \, \delta(\omega + \omega') \;\; , \tag{3.84}$$

$$\left\langle \Gamma^\dagger(\omega') \Gamma^\dagger(\omega) \right\rangle = \mathcal{N}_1^*(\omega) \, \delta(\omega + \omega') \;\; , \tag{3.85}$$

$$\left\langle \Gamma^\dagger(\omega') \Gamma(\omega) \right\rangle + \left\langle \Gamma(\omega') \Gamma^\dagger(\omega) \right\rangle = \mathcal{N}_2(\omega) \, \delta(\omega - \omega') \;\; , \tag{3.86}$$

and

$$\mathcal{N}_1(\omega) = 2W'W^*V \coth\frac{\beta\hbar\omega_0}{2} \ , \tag{3.87}$$

$$\mathcal{N}_2 = 2W'\left(|W+i\omega|^2 + |V|^2\right)\coth\frac{\beta\hbar\omega_0}{2} \ . \tag{3.88}$$

The frequency auto-correlation function of $X_{\phi_{\rm LO}}$ is related to the spectral density $P_{\phi_{\rm LO}}(\omega)$ by

$$\left\langle X_{\phi_{\rm LO}}(\omega')X_{\phi_{\rm LO}}(\omega)\right\rangle = P_{\phi_{\rm LO}}(\omega)\,\delta(\omega-\omega') \ , \tag{3.89}$$

thus one finds

$$\begin{aligned} P_{\phi_{\rm LO}}(\omega) = &\frac{e^{2i\phi_{\rm LO}}\mathcal{N}_1(\omega)}{(i\omega+\lambda_0)(i\omega+\lambda_1)(-i\omega+\lambda_0)(-i\omega+\lambda_1)} \\ &+ \frac{e^{-2i\phi_{\rm LO}}\mathcal{N}_1^*(\omega)}{(-i\omega+\lambda_0^*)(-i\omega+\lambda_1^*)(i\omega+\lambda_0^*)(i\omega+\lambda_1^*)} \\ &+ \frac{\mathcal{N}_2(\omega)}{(i\omega+\lambda_0^*)(i\omega+\lambda_1^*)(-i\omega+\lambda_0)(-i\omega+\lambda_1)} \ , \end{aligned} \tag{3.90}$$

or in terms of the factors W and V

$$\begin{aligned} P_{\phi_{\rm LO}}(\omega) = &\frac{e^{2i\phi_{\rm LO}}W^*V + e^{-2i\phi_{\rm LO}}WV^* + |W+i\omega|^2 + |V|^2}{(\omega-i\lambda_0)(\omega+i\lambda_0)(\omega-i\lambda_1)(\omega+i\lambda_1)} \\ &\times 2W'\coth\frac{\beta\hbar\omega}{2} \ . \end{aligned} \tag{3.91}$$

This expression is equivalent to $S_x(\delta)$ in section 3.6. The next expression $P_{\phi_{\rm LO}}(0)$ is equivalent to $S_x(0)$ in Eq. 3.20.

Spectral Density at $\omega = 0$

At frequency $\omega = 0$ one finds

$$P_{\phi_{\rm LO}}(0) = \frac{1+2\zeta\cos(\phi_{\rm LO}-\phi_0)+\zeta^2}{\left(1-\zeta^2\right)^2}\frac{2W'}{|W|^2}\coth\frac{\beta\hbar\omega_0}{2} \ , \tag{3.92}$$

where the phase factor ϕ_0 is defined in Eq. (3.103).

The largest value

$$[P_\phi(0)]_{\max} = \frac{1}{(1-\zeta)^2}\frac{2W'}{|W|^2}\coth\frac{\beta\hbar\omega_0}{2}\ , \tag{3.93}$$

is obtained when $\cos(\phi_{\rm LO}-\phi_0)=1$, and the smallest value

$$[P_\phi(0)]_{\min} = \frac{1}{(1+\zeta)^2}\frac{2W'}{|W|^2}\coth\frac{\beta\hbar\omega_0}{2}\ , \tag{3.94}$$

when $\cos(\phi_{\rm LO}-\phi_0)=-1$.

Integrated Spectral Density

The integral over all frequencies of the spectral density is easily calculated by employing the residue theorem

$$\frac{\int_{-\infty}^{\infty}P_{\phi_{\rm LO}}(\omega)\,{\rm d}\omega}{2\pi W'\coth\frac{\beta\hbar\omega_0}{2}} = \frac{e^{2i\phi_{\rm LO}}W^*V + e^{-2i\phi_{\rm LO}}WV^* + 2|W|^2}{\lambda_0\lambda_1(\lambda_0+\lambda_1)}\ . \tag{3.95}$$

Using Eqs. (3.64) and (3.65) one finds

$$\frac{1}{2\pi}\int_{-\infty}^{\infty}P_{\phi_{\rm LO}}(\omega)\,{\rm d}\omega = \frac{1+\zeta\cos(\phi_{\rm LO}-\phi_0)}{1-\zeta^2}\coth\frac{\beta\hbar\omega_0}{2}\ . \tag{3.96}$$

Thus, the integrated spectral density peaks and deeps simultaneously with $P_{\phi_{\rm LO}}(0)$.

3.8.7 Appendix - The Principal Axes

Here we show the calculation of the local principle axes. Along these directions, the fluctuations obtain their largest and smallest values.

Consider an expansion of the function Θ near a complex number Z

$$\Theta(Z+z,Z^*+z^*) = \Theta_0 + Wz + Vz^* + O\left(|z|^2\right)\ , \tag{3.97}$$

where $\Theta_0=\Theta_0(Z,Z^*)$, and W and V are given by Eqs. (3.47) and (3.48) respectively.

The transformation

$$\begin{pmatrix}\xi\\ \eta\end{pmatrix} = \frac{1}{2}\begin{pmatrix}e^{i\phi} & e^{-i\phi}\\ -ie^{i\phi} & ie^{-i\phi}\end{pmatrix}\begin{pmatrix}z\\ z^*\end{pmatrix}\ , \tag{3.98}$$

represents axes rotation with angle ϕ (ϕ is real). The inverse transformation is given by

$$\begin{pmatrix} z \\ z^* \end{pmatrix} = \begin{pmatrix} e^{-i\phi} & ie^{-i\phi} \\ e^{i\phi} & -ie^{i\phi} \end{pmatrix} \begin{pmatrix} \xi \\ \eta \end{pmatrix} . \tag{3.99}$$

Using this notation one finds

$$Wz + Vz^* = R_\xi \xi + R_\eta \eta , \tag{3.100}$$

where

$$R_\xi = We^{-i\phi} + Ve^{i\phi} , \tag{3.101}$$

$$R_\eta = i\left(We^{-i\phi} - Ve^{i\phi}\right) . \tag{3.102}$$

Principle axes are obtained by choosing $\phi = \phi_0$ where

$$e^{2i\phi_0} = \frac{WV^*}{|WV|} . \tag{3.103}$$

Thus, using the notation

$$\left(\frac{WV}{|WV|}\right)^{1/2} = e^{i\phi_a} , \tag{3.104}$$

one finds that in the reference frame of the principle axes the following hold

$$R_\xi = e^{i\phi_a}\left(|W| + |V|\right) , \tag{3.105}$$

$$R_\eta = ie^{i\phi_a}\left(|W| - |V|\right) , \tag{3.106}$$

and

$$Wz + Vz^* = e^{i\phi_a}\left[\left(|W| + |V|\right)\xi + i\left(|W| - |V|\right)\eta\right] . \tag{3.107}$$

Chapter 4

Measurement of High Intermodulation Gain

4.1 Introduction

In this chapter we experimentally study small signal amplification near the onset of Duffing bistability [33]. A large pump signal drives the resonator near the onset of bistability, enabling amplification of small signals in a narrow bandwidth. To first order, the amplification is inversely proportional to the frequency difference between the pump and the signal. We demonstrate experimentally high signal gain in this regime and compare with the theoretical predictions. We estimate the gain to be about 15dB for our device.

4.2 Experimental

As was described previously, the device under study is a nanomechanical resonator consists of a suspended doubly clamped AuPd beam, located adjacent to a static gate electrode. To investigate nonlinear amplification, the resonator is driven by an applied force $F(t) = f_p \cos(\omega_p t) + f_s \cos(\omega_s t + \varphi)$. This is achieved by applying a voltage of the form $V = V_{dc} + V_p \cos(\omega_p t) + V_s \cos(\omega_s t + \varphi)$ where V_{dc} is a dc bias and $V_s << V_p << V_{dc}$.

When the pump is tuned to the critical point ($\sigma = \sqrt{3}\omega_0/2Q$, $|a_p|^2 = 8/3\sqrt{3}\kappa Q$) and $\delta \to 0$, we expect high amplification of both signal and idler. As was shown in the previous chapter, in this limit

$$|a_s| \simeq |a_i| \simeq \frac{f_s}{2\omega_0 \delta} \ . \tag{4.1}$$

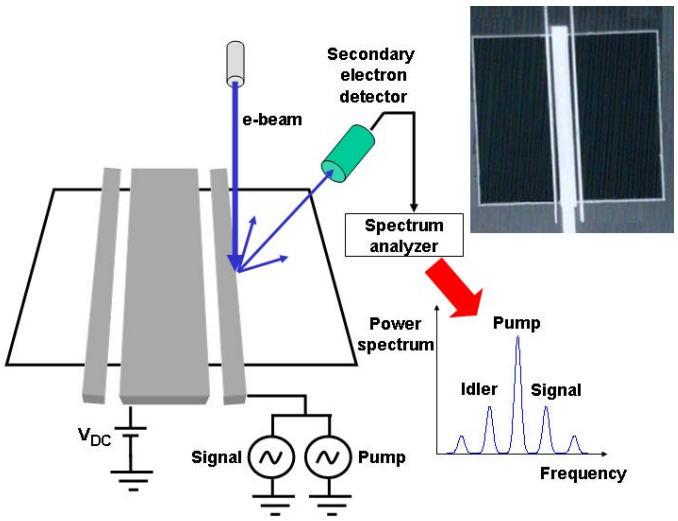

Figure 4.1: The experimental setup. The inset shows an electron micrograph of the device, consisting of two suspended doubly clamped nanomechanical resonators. Each resonator is of length l=100μm, width w=0.6μm, and thickness t=0.25μm, centered around a gate electrode with $d = 4\mu m$ gap. The device is mounted inside a SEM operated in a spot mode to detect the resonator's displacement. The displacement signal is probed by the secondary electrons detector and measured using a spectrum analyzer.

The experimental setup is shown in Fig. 4.1. In this case only, the measurement was done using the electron beam of the scanning electron microscope (SEM) where the imaging system of the microscope was employed for displacement detection (this is slightly different from the optical detection system which was described previously and was used in all the other measurements). The SEM is operated in a spot mode and the displacement signal (modulation of the number of secondary electrons) is probed by the secondary electrons detector and measured using a spectrum analyzer.

4.3 Results and Discussion

In the first measurement, the pump frequency is swept upward and then back downward while keeping δ constant. For each value of ω_p, the three spectral components of the pump, signal and idler (at frequencies ω_p, ω_s, and ω_i) of the displacement are measured using a spectrum analyzer.

A typical mechanical simultaneous response is shown in Fig. 4.2. As expected, we find hysteretic response and simultaneous jumps for the pump, signal, and idler spectral components.

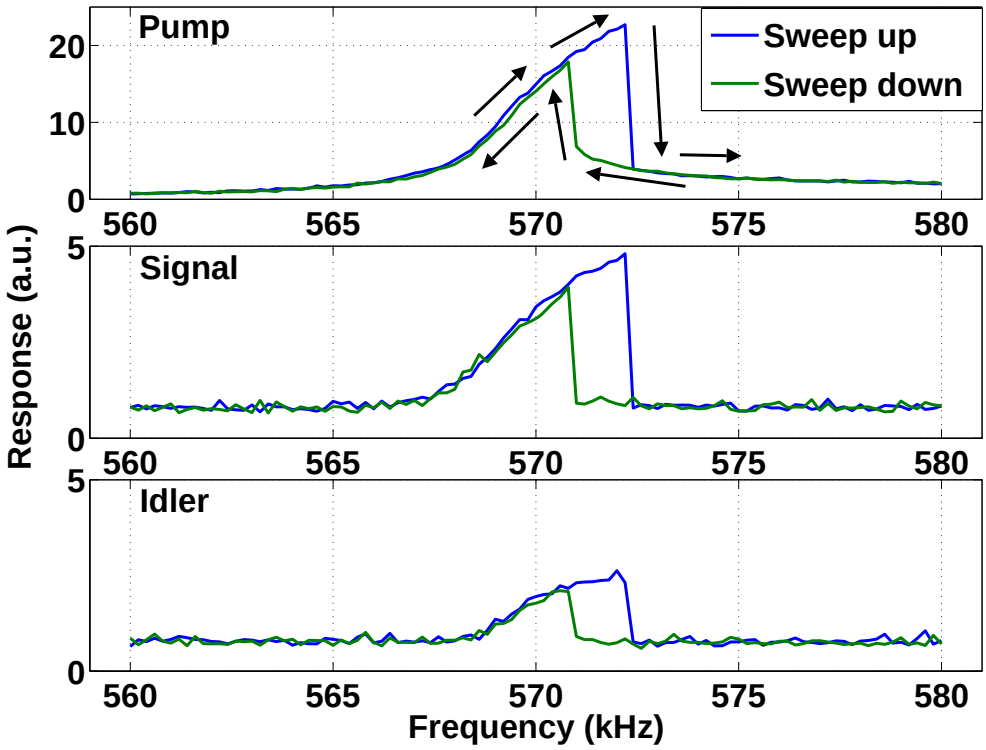

Figure 4.2: Simultaneous measurement of the pump, signal and idler spectral components of the mechanical displacement. The excitation frequency is swept upward (blue line) and downward (green line). The arrows in the pump's plot indicate the hysteresis loop. The excitation parameters are: pump ac voltage $V_p = 0.5\,\mathrm{V}$, $V_p/V_s = 6$, frequency offset $\delta/2\pi = 1\,\mathrm{kHz}$ and $V_{dc} = 5\,\mathrm{V}$. The horizontal axis is the pump frequency for all three plots. The pump signal and idler exhibit simultaneous jumps, as expected.

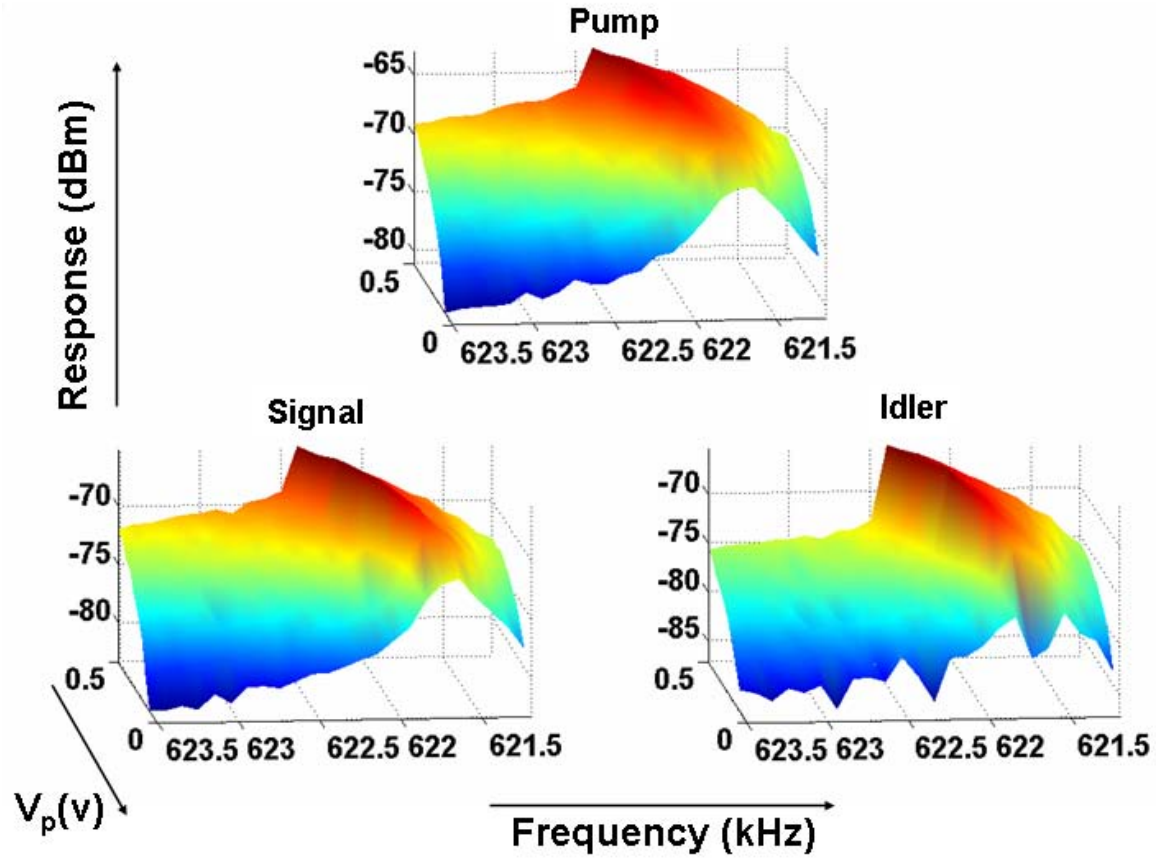

Figure 4.3: Mesh plots showing the response of the pump, signal and idler. The horizontal axis is the pump's frequency ω_p, the diagonal axis is the pump's ac voltage V_p, and the vertical axis is the response (displacement) axis in logarithmic scale. For each frequency, V_p is scanned from 0 to 0.5 V, $V_p/V_s = 6$, $\delta/2\pi = 100$ Hz, $V_{dc} = 5$ V. Note that the pump's response undergoes a jump along a line in the (V_p, ω_p) plane, starting from the bifurcation point. Along the same line, the spectral components of the signal and idler obtain their maximum value.

In Fig. 4.3, the mechanical responses of the pump, signal and idler are depicted as a function of the pump frequency $\omega_p/2\pi$ and the pump ac voltage V_p. For each frequency, the voltage V_p is scanned from 0 to 0.5 V. The results show good agreement with theory. As expected, we observe high signal amplification near the jump points. The amplification can be quantified using a logarithmic scale as

$$G \equiv 20 \log\left(\left|\frac{a_{s,pump\_on}}{a_{s,pump\_off}}\right|\right) . \tag{4.2}$$

The highest value of G, obtained near one of the jump points is 15dB. A comparison with theory is difficult since our model breaks down in the vicinity of the jump points as was explained above. Note, however, that this value is an underestimation of the actual gain due to the nonlinearity of our displacement detection scheme. Since the electron beam diameter is smaller than the displacement amplitude, the output signal is sublinear with respect to displacement.

Chapter 5

Noise Squeezing in a Nanomechanical Resonator

5.1 Introduction

In this chapter we study mechanical amplification and noise squeezing in a nonlinear nanomechanical resonator driven by an intense pump near its dynamical bifurcation point, namely, the onset of Duffing bistability [34]. Phase sensitive amplification is achieved by a homodyne detection scheme, where the displacement detector's output, which has correlated spectrum around the pump frequency, is down converted by mixing with a local oscillator operating at the pump frequency with an adjustable phase. The down converted signal at the mixer's output could be either amplified or deamplified, yielding noise squeezing, depending on the local oscillator phase.

In the previous chapter, we demonstrated high intermodulation gain by employing an intense pump signal to drive the resonator near the onset of bistability, enabling thus amplification of a small signal in a narrow bandwidth. Here we employ this mechanism for the first time in nanomechanical resonators to demonstrate experimentally phase sensitive amplification and noise squeezing. We coined this amplifier NanoMechanical Bifurcation Amplifier (NMBA).

5.2 Experimental

The experimental setup is shown in Fig. 5.1. The resonator is excited by two sources (pump and small test signal or noise) and its vibrations are detected optically. The photodetector signal is amplified, mixed with a local oscillator (LO), low pass filtered and measured by a spectrum analyzer.

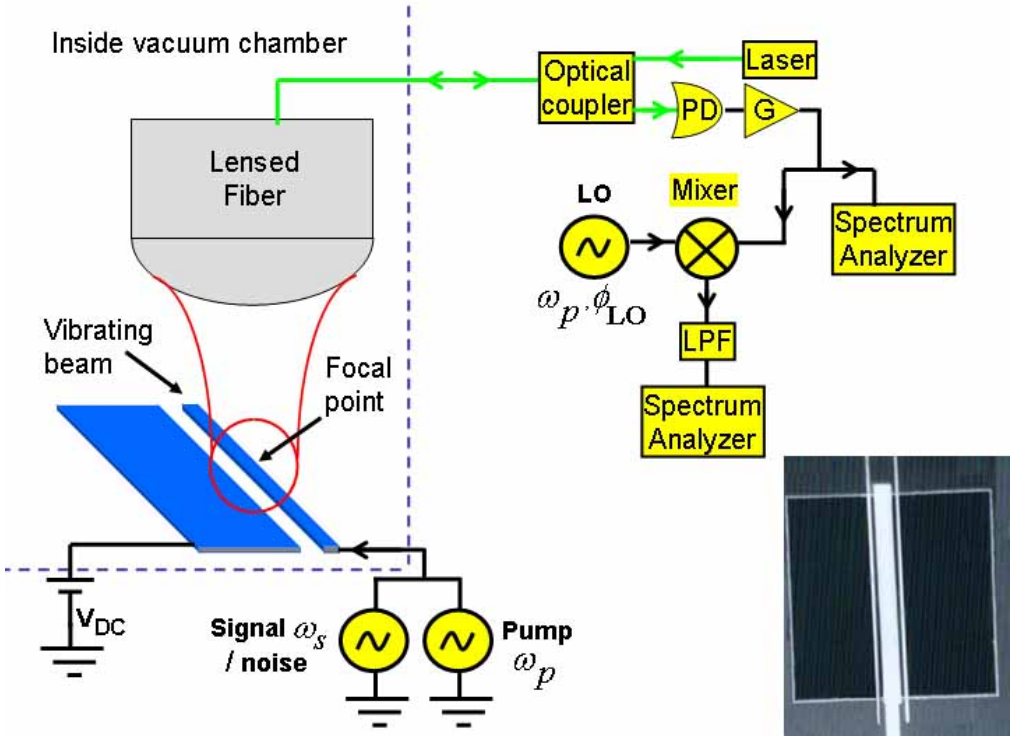

Figure 5.1: The experimental setup. The device consists of a suspended doubly clamped nanomechanical resonator. The resonator is excited by two phase locked sources (one source is used as a pump and the other one as a small test signal or as a noise source). The resonator's vibrations are detected optically. The inset shows an electron micrograph of the device.

As was explained previously, in order to investigate nonlinear amplification of a small test signal, the resonator is driven by an applied force $F(t) = f_p \cos(\omega_p t) + f_s \cos(\omega_s t + \varphi)$, $\omega_p = \omega_0 + \sigma$, amplitude f_p, and a weak *signal* with frequency $\omega_s = \omega_p + \delta$, relative phase φ, and amplitude f_s, where $f_s \ll f_p$ and $\sigma, \delta \ll \omega_0$. This is achieved by applying a voltage of the form $V = V_{dc} + V_p \cos(\omega_p t) + V_s \cos(\omega_s t + \varphi)$ where V_{dc} is a dc bias, $V_s \ll V_p \ll V_{dc}$. The resonator's displacement has spectral components at ω_p, ω_s, and at the intermodulations $\omega_p \pm k\delta$ where k is an integer, including the idler frequency $\omega_i = \omega_p - \delta$.

Strong correlation between the signal and the idler, occurring near the edge of the bistability region, could be exploited for phase sensitive amplification and noise squeezing [43, 70]. This is achieved by a homodyne detection scheme, where the displacement detector's output is down converted by mixing with a LO operating at frequency ω_p with an adjustable phase $\phi_{\rm LO}$ and phase locked to the pump. The mixer's output (IF port) has a spectral component $R(\delta)$ at frequency δ, which is proportional

to the phasor sum of the signal and the idler, yielding phase sensitive amplification, controlled by $\phi_{\rm LO}$. An example of a measurement of $R(\delta)$ vs. ϕ_{LO} is shown in Fig. 5.2(a). The factor $\Delta \equiv R(\delta)_{\rm max} - R(\delta)_{\rm min}$ characterizes the phase dependence of the amplification.

5.3 Results and Discussion

As a first step, we find the onset of bistability and characterize the bistability region. This is achieved by sweeping the pump frequency upward and back downward for different constant excitation amplitudes, without additional small signal or noise. Typical response curves were shown in Fig. 2.6. The bistability region and the bifurcation point $\rm B_p$ (marked with a circle) are shown in Fig. 5.2(b). The bistability region is found by calculating the difference between the two frequency responses (upward and downward sweeps). In the next step, we characterize small signal amplification by exciting the resonator with pump and small test signal where $V_p/V_s = 25$ and $\delta = 30\,\rm Hz$. Measurements of Δ vs. frequency are shown in Fig. 5.2(c) for four pump amplitudes (related to lines (1)-(4) in Fig. 5.2(b)). The response of the frequency upward (downward) sweep is depicted with black (green) line. For $V_p = 50\,\rm mV$ (Fig. 5.2(c)-1) the frequency sweep is contained within the monostable region and consequently the value of Δ is relatively small. For $V_p = 70\,\rm mV$ (Fig. 5.2(c)-2), $V_p = 90\,\rm mV$ (Fig. 5.2(c)-3), and $V_p = 110\,\rm mV$ (Fig 5.2(c)-4), on the other hand, the frequency sweeps cross the bistability region and two peaks are seen for Δ, corresponding to the jumps in the frequency response for the upward and downward frequency sweeps. These peaks originate from the high signal amplification in the jump points of the pump response. Note that in this case the width of the hysteresis loop (which is the distance between the peaks) is smaller relative to the case when the pump is the only excitation.

We now turn to investigate the resonator response to pump and noise. First, the bifurcation point ($\rm B_p$) is located. A frequency response of the beam, excited by the pump (without noise) in the vicinity of $\rm B_p$ is shown in Fig. 5.3(a). In the next step, the pump frequency is fixed to the bifurcation point and we add white noise to the excitation, having spectral density $S^{1/2}_{\rm Vnoise}$ =1 $\rm mV/\sqrt{Hz}$ (since the thermomechanical fluctuations are relatively weak, we employ externally injected noise).

The measured spectrum taken around the pump frequency (see Fig. 5.3(b)) demonstrates strong amplification occurring in this region, a manifestation of the noise rise phenomenon [74]. There is a good agreement between the theoretical fit (δ^{-1} dependence) to the experimental data for $\delta > 50\,\rm Hz$. For smaller values of δ the

model breaks down due to high order terms.

Noise squeezing is demonstrated in Fig. 5.4 where $\delta = 10\,\mathrm{Hz}$, $S_{Vnoise}^{1/2} = 1\,\mathrm{mV}/\sqrt{\mathrm{Hz}}$ and $S_x^{1/2}$ is plotted vs. the LO phase ϕ_{LO}. Here the sweep time is 6 s and the resolution bandwidth is 2 Hz. The blue line demonstrates the case where the pump is in the vicinity of the bifurcation point, whereas the green line demonstrates the case where the pump is far from the bifurcation point. The noise amplitude amplification is about 6. The deamplified (squeezed) quadrature is below the measurement noise floor, hence it can't be measured. Using the measured room temperature thermomechanical fluctuations, we estimate the noise floor (of the measurement system) to be $3.7 \times 10^{-13}\,\mathrm{m}/\sqrt{\mathrm{Hz}}$.

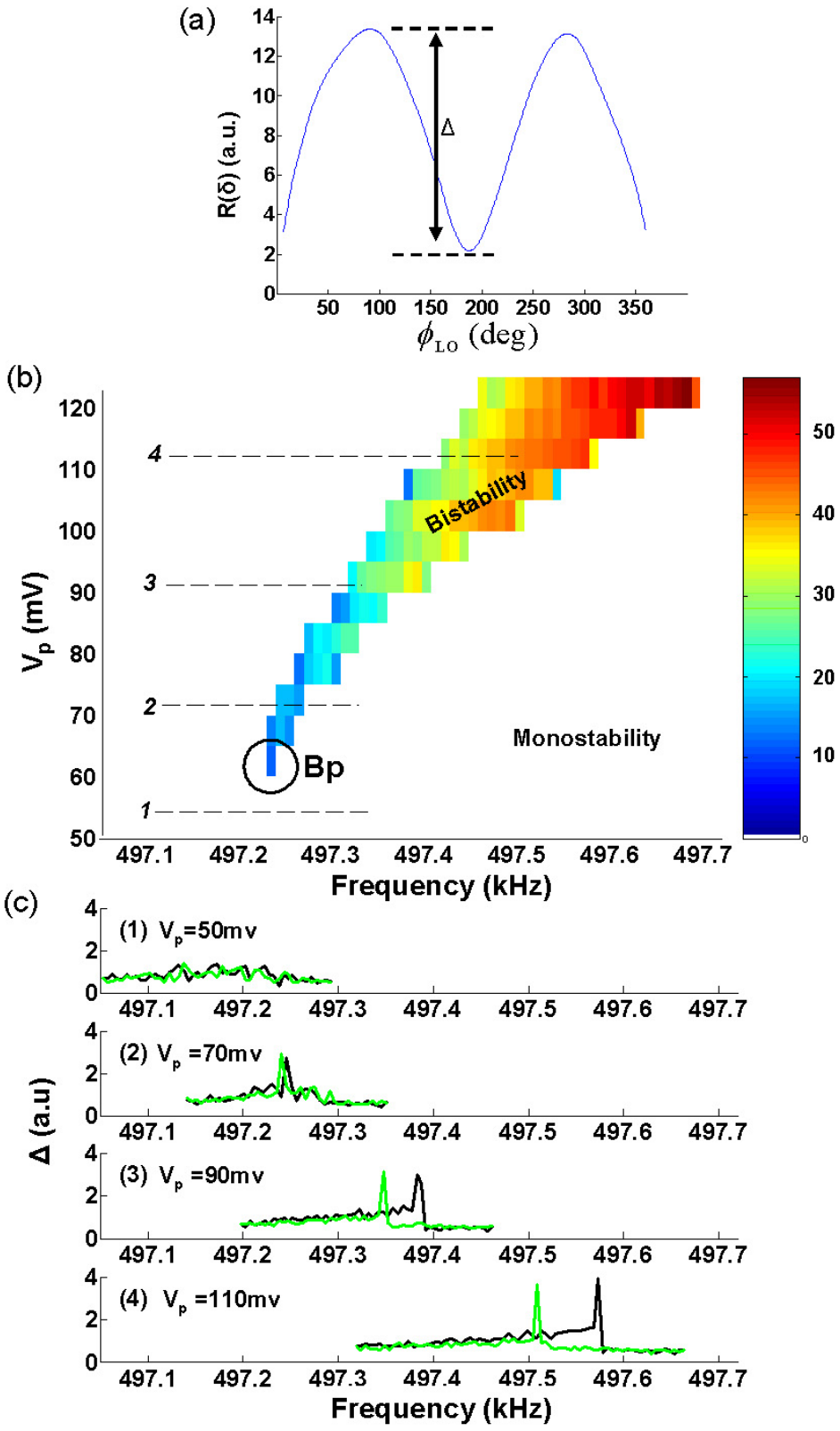

Figure 5.2: (a) Measured $R(\delta)$ vs. LO phase ϕ_{LO}. (b) Measurement of the bistability (hysteresis) region. The bifurcation point $\mathrm{B_p}$ is marked with a circle. (c) The parameter Δ vs. frequency for four different Vp values (related to lines (1)-(4) in Fig. 5.2(b)).

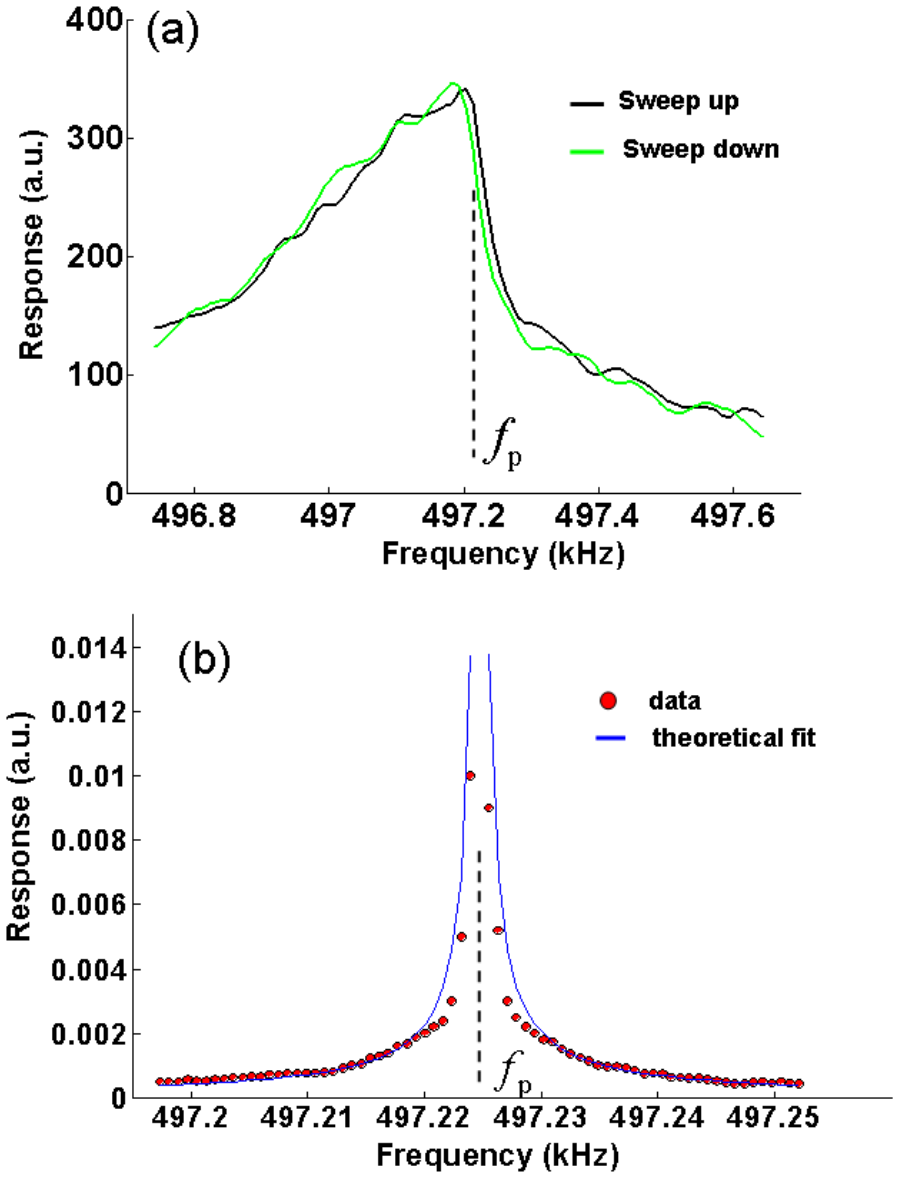

Figure 5.3: (a) Pump response near B_p. Upward and downward sweeps are seen in black and green respectively. (b) Averaged spectrum response for pump and noise excitation. The input noise spectral density is $1\,\mathrm{mV}/\sqrt{\mathrm{Hz}}$. Circles indicate the experimental data, whereas a theoretical fit is seen as a blue line.

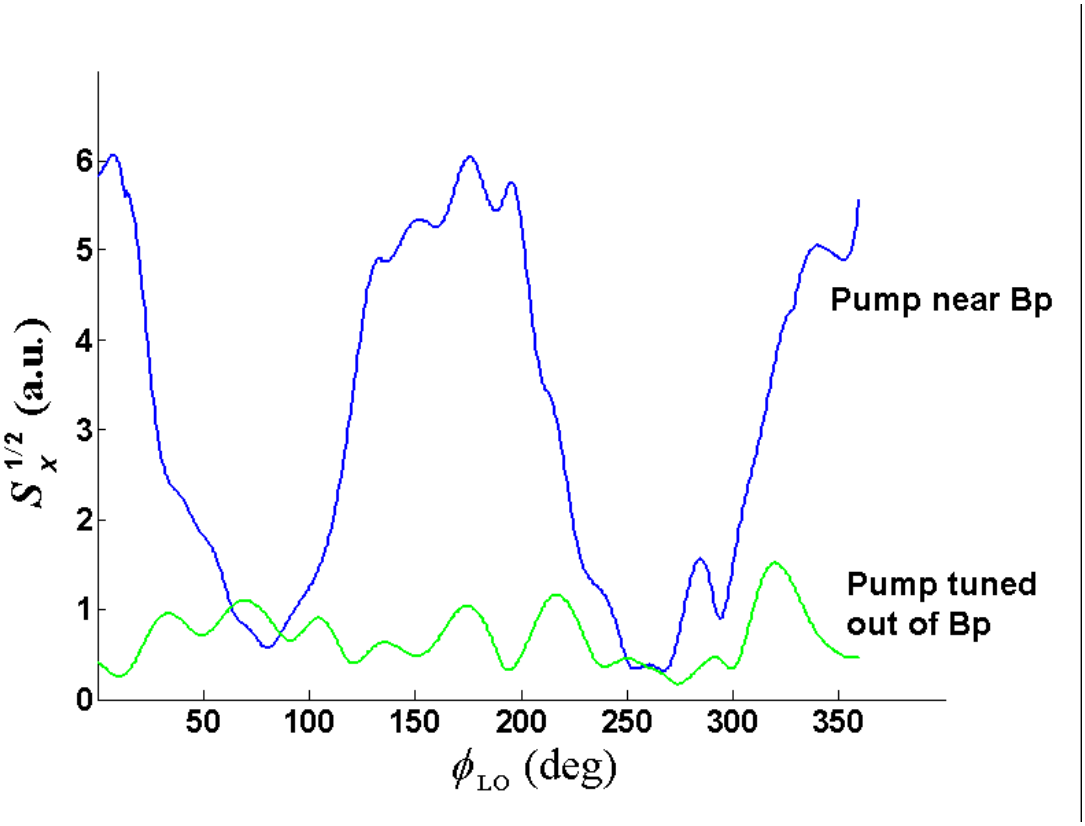

Figure 5.4: Noise squeezing. The spectral component $S_x^{1/2}$ vs. ϕ_{LO} for $\delta = 10\,\mathrm{Hz}$. The resonator is excited by pump and noise. Blue line - pump near Bp, green line - pump tuned out of Bp (200Hz higher).

Chapter 6

Signal Amplification via Stochastic Resonance

6.1 Introduction

In this chapter we experimentally study stochastic resonance (SR) in a nonlinear bistable nanomechanical resonator [35]. We compare our results to the theory of high frequency stochastic resonance. As in the previous chapters, the device consists of an AuPd doubly clamped beam serving as a nanomechanical resonator excited capacitively by an adjacent gate electrode and its vibrations are detected optically. The resonator is tuned to its bistability region by an intense pump near a point of equal transition rates between its two metastable oscillation states. The pump is AM modulated, inducing modulation of the activation barrier between the states. When noise is added to the excitation, the resonator's displacement exhibits noise dependent amplification. We measure the resonator's displacement in the time and frequency domains, the spectral amplification and the statistical distribution of the jump time.

SR is a phenomenon in which an appropriate amount of noise is used to amplify a periodic signal acting on a bistable nonlinear system. SR could be used as an amplification mechanism in nanomechanical devices in order to improve force detection sensitivity. Nanomechanical resonators operating in their nonlinear regime exhibit Duffing bistability, with low displacement amplitude state S_l and high displacement amplitude state S_h. In the presence of noise, the oscillator can occasionally overcome the activation barrier and hop between the states. When an oscillator is excited in the bistability region near a point of equal transition rates between its states, a response of an AM modulation of the pump force could be amplified by noise when the transition rate is comparable to twice the modulation frequency. This type of SR,

where the bistability property depends on the driving force (being higher than the critical force), is usually referred as "high frequency SR" [46],[62],.

Here we demonstrate high frequency SR in our nanomechanical resonator and measure the noise dependent amplification. Our study extends previous work [61]−[62] by characterizing SR by spectral amplification [76], and by measuring the statistical distribution of the jump time at SR condition.

6.2 Theory

In this section I will present the theory of high frequency stochastic resonance, based on the work done by Dykman *et. al.* [46],[75],[77].

Bistable systems are characterized by both local relaxation times t_{ri}, t_{rj} about their stable states i, j and by the average lifetimes $\langle T_i \rangle = W_{ij}^{-1}$, where W_{ij} are the $i \rightarrow j$ transition probabilities. Provided that $W_{ij}t_{ri}$, $W_{ji}t_{rj} << 1$, the concept of bistability is meaningful because a system will then spend most of the time fluctuating about one of the stable states. If its parameters pass through the range of bistability in a time much less than $\langle T_i \rangle$, the system will display hysteresis: it will tend to remain within one of the stable states. For fixed system parameters, however, over times $\tilde{} \langle T_i \rangle$ a fixed stationary distribution over the stable states is built up and the system forgets which of the stable states was occupied initially.

The transition probabilities W_{ij} of a system in thermal equilibrium is usually given by Kramer's (Arrhenius) law

$$W_{ij} \propto \exp(-E_a/T), \tag{6.1}$$

where T is the temperature and E_a is the characteristics activation energy of the transition $i \rightarrow j$. In the case of a Brownian particle, the quantity E_a is simply the depth of the potential well from which the particle escapes. For nonequilibrium systems, however, the calculation of the transition probabilities is a nontrivial problem. A rather general approach to its solution has been proposed for dynamical systems driven by external Gaussian noise. In this case

$$W_{ij} \propto \exp(-R/\alpha), \tag{6.2}$$

where α is the noise intensity and R is an activation energy of the transition $i \rightarrow j$, given by the solution of a certain variational problem.

In the general case of a bistable system, the characteristic activation energies R_1

and R_2 for the two transitions differ from one another. Consequently, for sufficiently weak noise, W_{12} and W_{21} differ exponentially. So also the stationary populations

$$w_1 = \frac{W_{21}}{W_{12} + W_{21}}; w_2 = \frac{W_{12}}{W_{12} + W_{21}}. \tag{6.3}$$

For most parameter values, the ratio w_1/w_2 is either exponentially small (for $R_2 - R_1 >> \alpha$) or large (for $R_1 - R_2 >> \alpha$) and the system occupies with an overwhelming probability the state 2 or 1, respectively. Only within a very narrow range of parameters where $|R_1 - R_2| \lesssim \alpha$, the populations w_1 and w_2 are of the same order of magnitude. In this range, a kinetic phase transition (KPT) occurs: the behavior of a noise driven dynamical system is to some extent analogous to that of a thermodynamic system with coexisting phases within the range of its first-order phase transition, where both phases are well manifested.

A well known signature of systems experiencing phase transition is the strong associated increase of fluctuations. The large occasional fluctuations between the stable states will give rise to intense and extremely narrow peak in the spectral density of fluctuations (SDF). A Brownian particle fluctuating in a symmetric double-well potential (that is, exactly at the phase transition point, $w_1 = w_2$), and driven by a low frequency periodic force, will exhibit stochastic resonance.

An important class of bistable systems is those that display bistability when driven by an intense periodic force, but which are monostable otherwise. The single well Duffing oscillator (as in our device) is an example of such a system. In this case, the fluctuational transitions between the stable states modulate the response of the system at the driving frequency. Extremely tall and narrow spectral peak is therefore to be expected in the SDF. Because the width of the peak increases exponentially with noise intensity, it is to be anticipated that the SNR for a signal at frequency close to the drive frequency will also increase with noise intensity, a manifestation of high frequency SR.

As in the previous chapters, consider the EOM

$$\ddot{x} + 2\mu\dot{x} + \omega_0^2(1 + \kappa x^2)x = f_p \cos(\omega_p t) + F_n(t), \tag{6.4}$$

where μ is the damping constant, $\omega_0/2\pi$ is the resonance frequency of the fundamental mode of the oscillator, and κ is the cubic nonlinear constant. The force $F_n(t)$ is a Gaussian white noise of characteristic intensity B such that

$$\langle F_n(t) F_n(t\prime)\rangle = 2\mu B\delta(t).$$

To be consistent with Dykman's notation, we will use the following complex dimensionless envelopes u and u^* and the dimensionless time τ,

$$x = (\frac{2\omega_p\sigma}{3\kappa\omega_0^2})^{1/2}(ue^{i\omega_p t} + u^*e^{-i\omega_p t}) \ , \tag{6.5}$$

$$\dot{x} = i\omega_p(\frac{2\omega_p\sigma}{3\kappa\omega_0^2})^{1/2}(ue^{i\omega_p t} - u^*e^{-i\omega_p t}) \ ,$$

$$\tau = |\sigma|\, t \ .$$

We will assume $\sigma = \omega_p - \omega_0, \kappa > 0$. The EOM in terms of the variable u from Eq. (6.4) - (6.5) takes the form

$$\frac{du}{d\tau} = v + \eta\tilde{f}(\tau), \tag{6.6}$$

$$v \equiv -\eta u + iu(|u|^2 - 1) - i\beta^{1/2} \ ,$$

where

$$\eta = \mu/\sigma \ , \ \beta = \frac{3\kappa\omega_0^2 f_p^2}{32\omega_p^3\sigma^3}.$$

The parameter η is the reduced damping coefficient and the parameter β is the dimensionless force intensity. The term $\tilde{f}(\tau)$ is a random force proportional to $F_n(t)$ in the EOM,

$$\tilde{f}(\tau) \equiv -i(\frac{3\kappa\omega_0^2}{8\omega_p^3\mu^2\sigma})^{1/2}\exp(-i\omega_p t)F_n(t). \tag{6.7}$$

since $\langle F_n(t)F_n(t\prime)\rangle = 2\mu B\delta(t)$, $\tilde{f}(\tau)$ is asymptotically two-component white noise, satisfying

$$\left\langle \tilde{f}(\tau)\tilde{f}^*(\tau\prime)\right\rangle = 4\alpha\delta(\tau - \tau\prime), \ \alpha \equiv \frac{3\kappa\omega_0^2 B}{16\omega_p^3\mu}. \tag{6.8}$$

Here α is the reduced noise intensity. We will assume the noise to be weak $\alpha << 1$. The dynamics of the oscillator depends on the values of the three dimensionless parameters η, β, and α.

6.2.1 Transition probabilities and the spectral density of fluctuations

The most obvious effects of noise on the behavior of the oscillator are, first, the onset of fluctuations about the stable states and, second, the occurrence of fluctuation-induced transition between the states. Provided that the noise is weak, the system will spend most of its time in the close vicinity of one the stable states. Only very rarely will a sufficiently large fluctuation occur to cause a transition to the other stable state. As

was stated above, the dependence of the probability W_{ij} of the transitions on the noise intensity is of the activation type $W_{ij} \propto \exp(-R_i/\alpha)$. The activation energy R_i for the transition from state i is given by the solution of a variational problem [75], based on an idea due to Feynman. His suggestion was that there was a direct relationship between the probability density of the paths of the noise driven system and the noise itself. This inter-relationship allows us to write immediately, to logarithmic accuracy, the probability density functional for the paths of the system and to set up the variational formulation giving the most probable paths for first reaching a given point in the phase space of the system and for the transitions between the stable states. In the white noise case under consideration, the activation energy R_i is given [75], by the following variational problem:

$$R_i = \frac{1}{4}\min \int_{-\infty}^{\infty} \left|\tilde{f}(\tau)\right|^2 d\tau = \frac{1}{4}\eta^{-2}\min \int_{-\infty}^{\infty} d\tau \left|(\frac{du}{d\tau} - v)\right|^2 \tag{6.9}$$

$$u(-\infty) = u_i \ , \ u(\infty) = u_s$$

where u_i and u_s are the values u for the initially occupied stable state and for the saddle point, respectively.

In obtaining a variational (Euler) equation for the problem in Eq. 6.9, u and u^* should be varied independently. The resulting equation can be seen to be of the form

$$\frac{d^2u}{d\tau^2} - 2i\frac{du}{d\tau}(2\left|u\right|^2 - 1) - \eta^2 u\nu^2 + \sqrt{\beta}(2\left|u\right|^2 + u^2 - 1 - i\eta) = 0 \ , \tag{6.10}$$

where

$$\nu^2 \equiv 1 + \eta^{-2}(\left|u\right|^2 - 1)(3\left|u\right|^2 - 1),$$

together with the conjugate equation for u^*. These equations describe the conservative motion of an auxiliary system with two degree of freedom, in which a charged particle is moving in an electric potential and a magnetic field (appendix of [46]). The resultant dependences of R_i on β for lower and higher amplitudes of forced vibrations were numerically calculated in Ref. [46]. As expected, R_1 decreases and R_2 increases monotonically with increasing force intensity β. In the vicinity of the KPT point, R_1 and R_2 are nearly equal.

A revealing characteristic property of a fluctuating system is its spectral density

of fluctuations $S(\omega)$, given by $S(\omega) = \frac{1}{\pi}\,\mathrm{Re}\int_0^\infty dt\ exp(i\omega t)X(t)$, where

$$X(t) = \lim_{T\to\infty}\frac{1}{2T}\int_{-T}^{T} d\tau[x(t+\tau) - \langle x(t+\tau)\rangle] \times [x(\tau) - \langle x(\tau)\rangle].$$

In the case of weak noise, two principal contributions to $S(\omega)$ can be identified. The first arises from small fluctuations about the stable states. It is equal to the sum over the states j of the corresponding partial SDF's $S_j(\omega)$, weighted by the state populations w_j. The second contribution $S_{tr}(\omega)$ comes from the (relatively infrequent) fluctuational transitions between the states. Thus

$$S(\omega) = \sum_j w_j S_j(\omega) + S_{tr}(\omega). \tag{6.11}$$

The interesting part in our case is $S_{tr}(\omega)$. $S_{tr}(\omega)$ can readily be calculated if one notes that the populations w_j of the stable states fluctuate in time with a characteristic relaxation time $(W_{12} + W_{21})^{-1}$, so that dw_1/dt is given by the following rate equation

$$\frac{dw_1(t)}{dt} = -W_{12}w_1(t) + W_{21}w_2(t) = -(W_{12} + W_{21})w_1(t) + W_{21}\ , \tag{6.12}$$

$$w_1(t) + w_2(t) = 1$$

(The values of w_j appearing in 6.3 correspond to the stationary solution of 6.12). In the case of weak noise, these fluctuations can be shown [77] to result in a contribution to $S(\omega)$ of

$$S_{tr}(\omega) = \frac{2\omega_p\sigma}{3\pi\kappa\omega_0^2}\left|\langle u_1\rangle - \langle u_2\rangle\right|^2 w_1 w_2 \times \frac{W_{12} + W_{21}}{(W_{12} + W_{21})^2 + (\omega - \omega_F)^2}. \tag{6.13}$$

Here $\langle u_j\rangle$ denotes the ensemble average value of u in the state j, which in the zero noise limit is simply u_j. The spectral peak $S_{tr}(\omega)$ is extremely narrow: its width is determined by the transition probabilities, so that it is exponentially small and much smaller than the damping parameter μ. The product w_1w_2 which determines the intensity of $S_{tr}(\omega)$ is exponentially small for almost all values of β, η, with the exception of those within the very narrow range of the KPT (the phase-transition region) where $w_1 \sim w_2 \sim 1/2$. Thus, the onset of fluctuational transition-induced spectral peak is a specific phase-transition phenomenon.

6.2.2 High Frequency Stochastic Resonance

Consider now a system which is drived by a strong pump and additional weak trial force $f_s \exp(-i\omega_s t)$, as in the previous chapters. The most pronounced response to this weak force will be at frequency ω_s and at the idler frequency $\omega_i = 2\omega_p - \omega_s$. The modification to the ensemble averaged coordinate x is in the form

$$\delta \langle x(t) \rangle \simeq \chi_s(\omega_s) f_s \exp(-i\omega_s t) + \chi_i(\omega_i) f_s \exp(-i\omega_i t) \tag{6.14}$$

Here the oscillator response is characterized by two coefficients $\chi_s(\omega_s)$ and $\chi_i(\omega_i)$ which play the role of generalized susceptibilities. In the vicinity of the KPT, interesting features occur to this susceptibilities. If the noise is weak, the main effects of the additional force are: (1) to cause small amplitude periodic vibrations of u about their stable values, and (2) via the change in the probabilities of fluctuational transitions to modulate periodically the populations of the stable states. These effects give rise to expressions for the generalized susceptibilities of the form similar to Eq. 6.11.

$$\chi_s(\omega_s) = \sum_j w_j \chi_{s,j}(\omega_s) + \chi_{s,\,tr}(\omega_s) \tag{6.15}$$

with a similar expression for $\chi_i(\omega_i)$. Here $\chi_{s,j}(\omega_s)$ is the partial susceptibility related to the corresponding vibrations about the stable states. The partial susceptibilities can readily be calculated by linearizing the EOM for u. To first order, $\chi_{s,j}(\omega_s)$ and $\chi_{i,j}(\omega_i)$ are independent of noise.

We will be interested in the parts $\chi_{s,\,tr}(\omega_s)$ and $\chi_{i,\,tr}(\omega_i)$ that are related to the trial force induced redistribution over the states.

The effective modulation of the transition probabilities by the trial force arises when its frequency ω_s is very close to ω_p, that is $\omega_p - \omega_s << \mu$. In this case, the trial force smoothly raises and lowers the effective "barrier" between the stable states with the period $2\pi/(\omega_p - \omega_s)$, so that the activation energies R_1 and R_2 of the fluctuational transitions vary periodically in time. In turn, they give rise to periodic additions to the transitions probabilities W_{ij} and hence to the populations w_j of the stable states. The final expressions for the redistribution-induced additions to the generalized susceptibilities are [46]

$$\chi_{s,\,tr}(\omega_s) = \frac{w_1 w_2}{2\omega_p \sigma}(\langle u_1^* \rangle - \langle u_2^* \rangle)(\frac{\lambda_1 - \lambda_2}{\alpha}) \times \left[1 + \frac{i(\omega_p - \omega_s)}{W_{12} + W_{21}}\right]^{-1},$$

$$\chi_{i,\,tr}(\omega_i) = \frac{\langle u_1 \rangle - \langle u_2 \rangle}{\langle u_1^* \rangle - \langle u_2^* \rangle} \chi_{s,\,tr}(\omega_s), \tag{6.16}$$

$$\lambda_j \equiv \sqrt{\beta}(\frac{\partial R_j}{\partial \beta}) \quad j = 1, 2.$$

It is evident from Eq. 6.16 that the susceptibilities $\chi_{s,\,tr}(\omega_s)$ and $\chi_{i,\,tr}(\omega_i)$ are large only within the range of parameters β, η, close to the KPT, where the populations w_1, w_2 of the stable states are of the same order of magnitude. The characteristic range of the frequency ω_s of the trial force within which this susceptibilities are large is determined by the transition probabilities. Consequently, it increases exponentially with increasing noise intensity. This property gives rise to stochastic resonance, *i.e.*, to an increase of the SNR with increasing noise. The common figure of merit to characterize the SNR when dealing with SR is the ratio between the power spectral peak $\frac{1}{4}f_s^2\left|\chi_s(\omega_s)\right|^2$ (or $\frac{1}{4}f_s^2\left|\chi_i(\omega_i)\right|^2$) to the background power spectral density $S(\omega_s)$ (or $S(\omega_i)$).

$$SNR(\omega_s) \equiv \frac{\frac{1}{4}f_s^2\left|\chi_s(\omega_s)\right|^2}{S(\omega_s)} \; ; \; SNR(\omega_i) \equiv \frac{\frac{1}{4}f_s^2\left|\chi_i(\omega_i)\right|^2}{S(\omega_i)}$$

Since $\chi_{s,j}(\omega_s)$ and $\chi_{i,j}(\omega_i)$ are independent of noise for weak noise whereas the partial contributions to the SDF $S_j(\omega)$ increase linearly with the noise intensity, far from the KPT, where the fluctuational transitions contributions to the susceptibilities and SDF are small, the SNR decrease with increasing noise. Within the phase-transition range, on the other hand, the main contribution to $\chi_s(\omega_s)$, $\chi_i(\omega_i)$ and $S(\omega)$ comes from the states transitions parts. This is because their ratio to the corresponding partial contributions is inversely proportional to $\alpha << 1$, in the case of $\chi_s(\omega_s)$, $\chi_i(\omega_i)$, and to $W_{ij}/\mu << 1$ in the case of $S_j(\omega)$. In this case the SNR will be given by [46]

$$SNR_{tr}(\omega_s) = \; SNR_{tr}(\omega_i) = f_s^2\frac{3\pi\kappa\omega_0^2}{32\omega_p^3\sigma^3}(\frac{\lambda_1-\lambda_2}{\alpha})^2 \times \frac{W_{12}W_{21}}{W_{12}+W_{21}} \tag{6.17}$$

Since $W_{ij} \propto \exp(-R_i/\alpha)$, the quantities SNR_{tr} increase exponentially with increasing noise intensity. This implies the onset of high-frequency SR within the KPT range. When the noise intensity getting higher, the weak noise assumption is not valid and the signal is screened by the noise.

6.3 Experimental

A schematic diagram of the experimental setup employed for measuring SR is depicted in Fig. 6.1. The resonator is excited by two sources (pump and noise) and its vibrations are detected optically. To measure the time trace, the photodetector signal is amplified, mixed with a local oscillator (LO), and low pass filtered. The spectrum around ω_p of the amplified PD signal is measured using a spectrum analyzer.

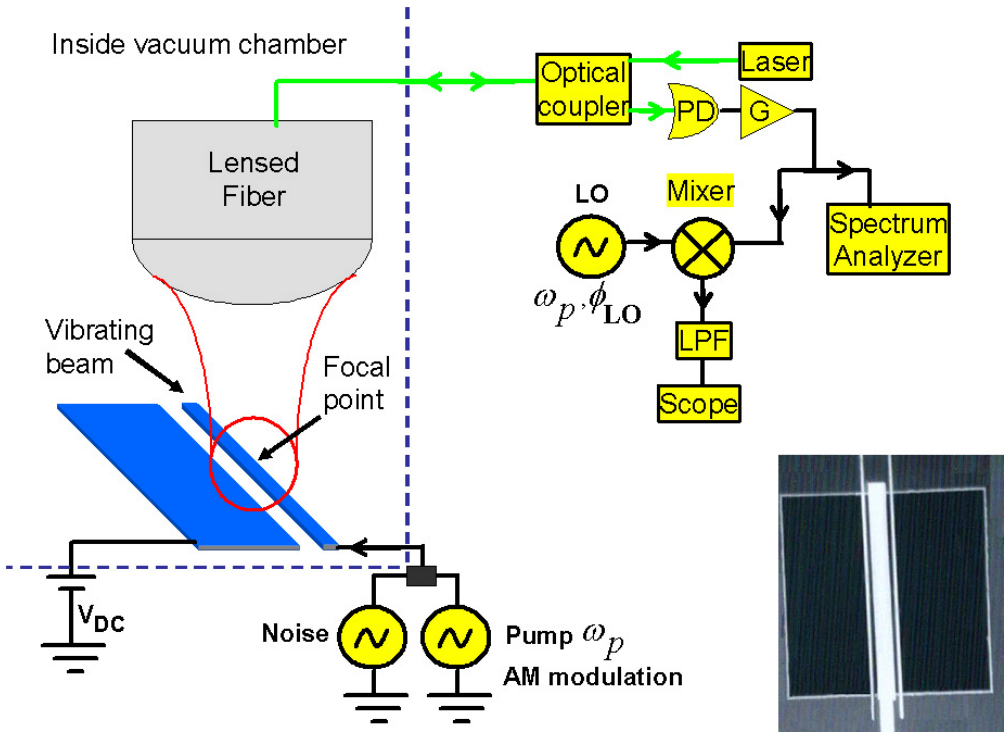

Figure 6.1: The experimental setup. The device consists of a suspended doubly clamped nanomechanical resonator. The resonator is excited by two arbitrary waveform generators (one is used for the pump and the second for the noise). The resonator's vibrations are detected optically. The inset shows an electron micrograph of the device.

6.4 Stochastic Resonance

The bistability region of the device is found by exciting the resonator with a harmonic pump signal, sweeping its amplitude upward and then back downward for constant pump frequency (in opposite to the previous chapters where the excitation amplitude has been held constant and the pump frequency has been swept), calculating the difference between the two responses, and repeating for a range of frequencies. The result is shown in Fig. 6.2a. An example of a pump amplitude hysteresis loop for a constant pump frequency of 520.58 kHz (the broken line in Fig. 6.2a) is shown in Fig. 6.2b. When the pump is AM modulated without additional noise, the resonator will respond with small amplitude oscillation following the amplitude response curve in the respective hysteresis branch (vertical black line in Fig. 6.2b). To bring the system into SR, the resonator is tuned to its bistability region by an intense pump near a point of equal transition rates between its states. Next, the pump is AM modulated, inducing modulation of the activation barrier between the states and modulating the

transition rates Γ_1 and Γ_2 of the transitions $S_l \rightarrow S_h$ and $S_h \rightarrow S_l$ respectively, in the presence of noise. Here we use the symbols Γ_1 and Γ_2 instead of W_{12} and W_{12} , respectively. When an appropriate amount of noise is added, the resonator will hop

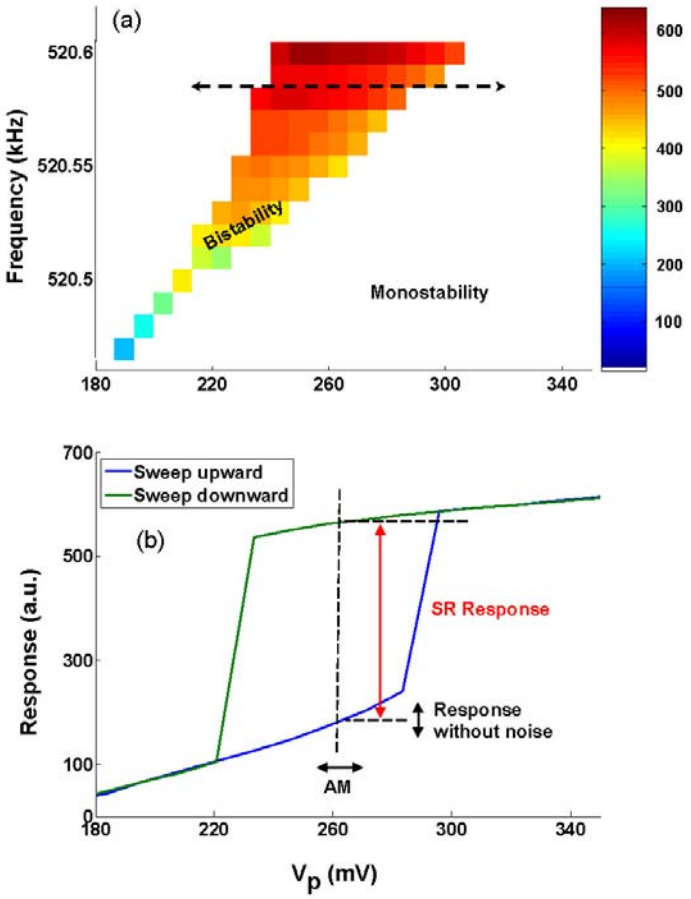

Figure 6.2: (a) Measurement of the bistability region. (b) Pump amplitude hysteresis loop for a constant pump frequency of 520.58 kHz (the broken line in Fig. 1a). The vertical arrows show the response to a small AM modulation (horizontal arrow).

from one state to the other in synchronization with the modulation and with large amplitude (vertical red line in Fig. 6.2b). The working point (pump amplitude and frequency) is determined such that $\Gamma_1 \simeq \Gamma_2$.

The resonator is excited by an applied force $F(t) = f_p(1 + A_{\rm mod}\cos\Omega t)\cos(\omega_p t) + F_n(t)$ composed of an AM modulated pump signal with amplitude f_p, frequency ω_p, modulation frequency Ω and modulation depth $A_{\rm mod}$, and $F_{\rm n}(t)$ is a zero-mean Gaussian white noise with autocorrelation function $\langle F_{\rm n}(t)F_{\rm n}(0)\rangle = 2D\delta(t)$ where D is the noise intensity. This is achieved by applying a voltage of the form $V = V_{dc} + V_p(1 + A_{\rm mod}\cos\Omega t)\cos(\omega_p t) + V_n(t)$ where V_{dc} is a dc bias, V_p is the pump

amplitude, and $V_n(t)$ is the applied voltage noise. The voltage noise intensity is $I \equiv \langle V_n^2(t)\rangle^{1/2}$ and $V_p, I \ll V_{dc}$.

The displacement spectral density can be expressed as

$$S_x(\omega) = \sum_{k=-\infty}^{k=\infty} A_k(D)\delta(\omega_p + k\Omega) + S_{nx}(\omega), \tag{6.18}$$

composed of delta peaks at the mixing products $\omega_p + k\Omega$, $k = 0, \pm1, \pm2...$, and a background spectral density of the noise denoted by $S_{nx}(\omega)$. In order to characterize the noise dependent amplification, we define a spectral amplification parameter η_k by

$$\eta_k(D) = A_k(D)/A_k(D=0). \tag{6.19}$$

6.5 Results and Discussion

Typical results of SR measured in the time and frequency domains are shown at the left and right sides of Fig. 6.3 for five voltage noise intensities (panels (a)-(e)). Here Ω=20 Hz, $A_{\rm mod} = 10\%$, and $V_{dc} = 25$ V. The blue dotted line drawn in the time domain represents the modulation signal. The voltage noise intensities (a) 1 mV and (b) 349 mV correspond to low noise levels below the SR value. Panel (a) shows response without jumps. Panel (b) shows the response containing few arbitrary jumps. The voltage noise intensity (c) 464 mV correspond to SR condition where every half cycle, the resonator jumps to the other metastable state. The voltage noise intensities (d) 530 mV and (e) 600 mV are higher than the SR value. In panel (d), as in ref [61], the resonator stays in the S_l state with few jumps to the S_h state. In panel (e), the high noise almost completely screens the signal. In the frequency domain displayed at the right side of Fig. 6.3, the fundamental frequency and the mixing products can be seen. At SR, the spectrum contains high order mixing products.

The dependence of the spectral amplification $\eta_k(D)$ ($k = \pm1$ and $k = \pm3$) on voltage noise intensity I is shown in Fig. 6.4a and Fig. 6.4b respectively. Here $\Omega = 30$ Hz, $A_{\rm mod} = 10\%$, and the optimal noise intensity for maximal amplification $I = 750$ mV. The amplification $\eta_{\pm1}$have maximal value of 5 while $\eta_{\pm3}$ have maximal value of 40.

The dependence of the spectral amplification $\eta_3(D)$ on I for three AM frequencies $\Omega = 20$ Hz ,30 Hz, and 40 Hz is shown in Fig. 6.4c for $A_{\rm mod} = 10\%$. As predicted theoretically [76], amplification is monotonically decreasing with Ω.

Our results have good agreement with theory. As expected, the spectral ampli-

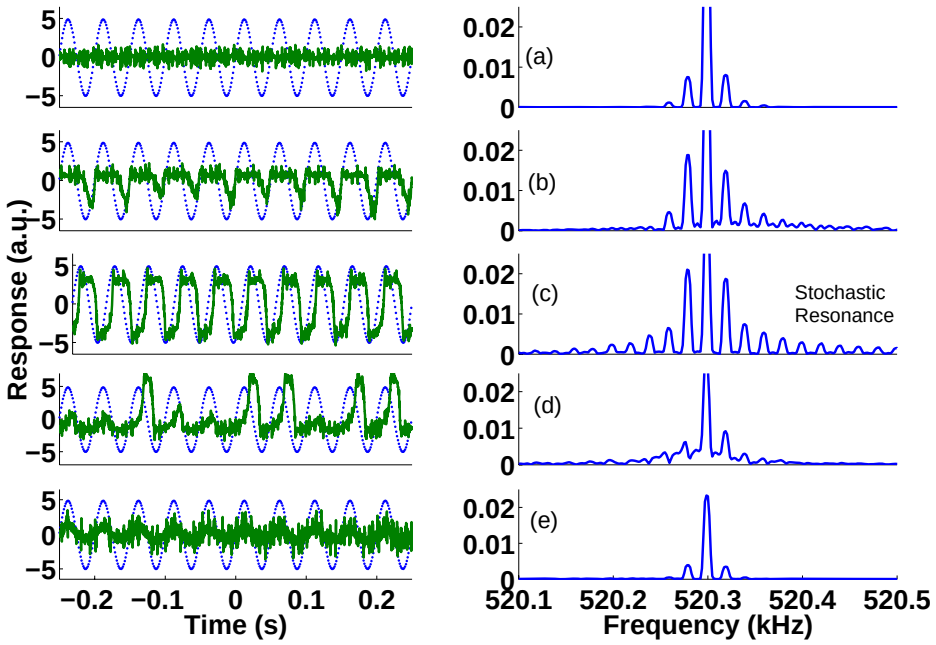

Figure 6.3: Panels $(a)-(e)$ exhibit typical snapshots of the resonator's response in the time domain (left) and in the frequency domain (right) as the input voltage noise intensity is increased. The dotted line in the time domain represents the modulation signal.

fication each rise and fall with increasing noise intensity with well defined maxima, thereby confirming the occurrence of HFSR.

6.6 An Example of transition rate calculation

Finally, we demonstrate the method proposed in ref. [78] for extracting transition rates from SR measurements.

Assume that at time $t = -t_0$ the system is in state S_l, where $t_0 > 0$. The transition rate Γ of the process $S_l \rightarrow S_h$ depends on an externally applied time varying parameter $p\,(t)$ (the amplitude modulation of the pump in our case). Further, assume that for p close to some fixed value p_{m} the transition rate is given approximately by

$$\Gamma\,(p) = \Gamma_{\mathrm{m}} \exp\left(-\kappa^2 \frac{p - p_{\mathrm{m}}}{p_{\mathrm{m}}}\right) , \tag{6.20}$$

where both Γ_{m} and κ are positive constants.

The probability distribution function $F\,(\tau)$ for a transition of the kind $S_l \rightarrow S_h$ to

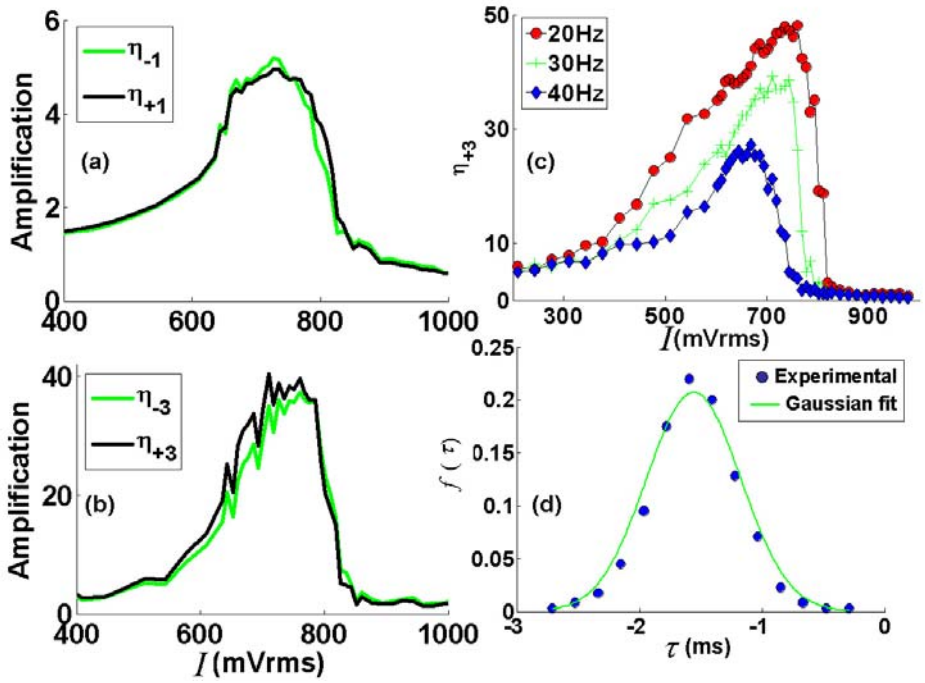

Figure 6.4: Panels (a),(b) spectral amplification $\eta_k(D)$ ($k = \pm 1$ and $k = \pm 3$) vs. voltage noise intensity. (c) The spectral amplification $\eta_{+3}(D)$ vs. noise intensity for three AM frequencies. (d) Measurement of the probability density $f(\tau)$, where τ is the difference between the time of the transition $S_l \to S_h$ and the time at which the modulation amplitude gets its maximal value.

take place within the time interval $(-t_0, \tau)$ is given by

$$F(\tau) = \int_{-t_0}^{\tau} f(t)\,\mathrm{d}t\ , \tag{6.21}$$

where $f(\tau)$ is the corresponding probability density. By definition, the following holds

$$\frac{f(\tau)}{1 - F(\tau)} = \Gamma\left[p(\tau)\right]\ . \tag{6.22}$$

The initial condition $F(-t_0) = 0$ and Eq. (6.22) yield

$$f(\tau) = \Gamma\left[p(\tau)\right] \exp\left(-\int_{-t_0}^{\tau} \Gamma\left[p(t)\right] \mathrm{d}t\right)\ . \tag{6.23}$$

Further assume the case where at time $t = 0$ the function $p(t)$ obtains a local minimum $p(0) = p_{\mathrm{m}}$. Near $t = 0$ one has

$$p(t) = p_{\mathrm{m}}\left(1 + \Omega^2 t^2\right) + O\left(t^3\right)\ . \tag{6.24}$$

Thus, in the vicinity of $t = 0$ Eq. (6.20) becomes

$$\Gamma(t) = \Gamma_{\mathrm{m}} \exp\left(-\kappa^2 \Omega^2 t^2\right) , \tag{6.25}$$

and the following holds

$$f(\tau) = \Gamma_{\mathrm{m}} \exp\left(-\kappa^2 \Omega^2 \tau^2 - \sqrt{\pi}\frac{\Gamma_{\mathrm{m}}}{\kappa\Omega}\frac{\mathrm{erf}(\kappa\Omega\tau) + \mathrm{erf}(\kappa\Omega t_0)}{2}\right) . \tag{6.26}$$

Keeping terms up to second order in $\kappa\Omega\tau$ and assuming the case where

$$\left(-\kappa\Omega t_0 + \frac{\Gamma_{\mathrm{m}}}{2\kappa\Omega}\right)^2 \gg 1 , \tag{6.27}$$

allow approximating the probability density $f(\tau)$ by

$$f(\tau) = \frac{\Omega\kappa}{\sqrt{\pi}} \exp\left[-\kappa^2\Omega^2\left(\tau + \frac{\Gamma_{\mathrm{m}}}{2\kappa^2\Omega^2}\right)^2\right] . \tag{6.28}$$

In this approximation the random variable τ has a normal distribution function with a mean value

$$\mu_\tau = -\frac{\Gamma_{\mathrm{m}}}{2\kappa^2\Omega^2} , \tag{6.29}$$

and a variance

$$\sigma_\tau^2 = \frac{1}{2\kappa^2\Omega^2} . \tag{6.30}$$

Whereas, the parameters Γ_{m} and κ, are given by

$$\Gamma_{\mathrm{m}} = -\frac{\mu_\tau}{\sigma_\tau^2} , \tag{6.31}$$

and

$$\kappa^2 = \frac{1}{2\sigma_\tau^2\Omega^2} . \tag{6.32}$$

Lets return now to our experiment. Near the maximum (minimum) points of the amplitude modulation signal, the rate Γ_1 (Γ_2) obtains its largest value, which is denoted by Γ_{m1} (Γ_{m2}). Let τ be the difference between the time of the transition $S_l \rightarrow S_h$ and the time at which the modulation amplitude gets its maximal value

(namely, the time at which $\Gamma_1 = \Gamma_{m1}$). The probability density of the random variable τ is now $f(\tau)$. The measured probability density $f(\tau)$, derived from 1000 modulation cycles sampled in the time domain is shown in Fig. 6.4d. The solid line represents a Gaussian function fitted to the measured probability density. The rate Γ_{m1} can be estimated from the expectation value μ_τ and the variance σ_τ^2 of τ by $\Gamma_{m1} = -\mu_\tau/\sigma_\tau^2$, yielding $\Gamma_{m1} = 10.49\,\mathrm{kHz}$.

In conclusion, stochastic resonance has been demonstrated in a nanomechanical resonator. The resonator was tuned to its bistability region by an intense pump near a point of equal transition rates between its states. An AM modulation is used to modulate the activation barrier between the states. When noise is injected, the resonator's response exhibits noise dependent amplification. We measure the resonator's displacement in the time and frequency domains, the spectral amplification and statistics of the jumps time. SR could be very useful in nanomechanical devices as a mean to implement on-chip mechanical amplification and to increase the signal to noise ratio.

Chapter 7

Summary

In this work we have studied the nonlinear dynamics of nanomechanical resonators and exploited it for novel on-chip mechanical amplification schemes.

We have studied mechanical amplification and noise squeezing in a nonlinear nanomechanical resonator driven by an intense pump near its dynamical bifurcation point, the onset of Duffing bistability, enabling thus amplification of a small signal in a narrow bandwidth. We have demonstrated high intermodulation gain and phase sensitive amplification. We employ bifurcation amplification for the first time in nanomechanical resonators to demonstrate experimentally phase sensitive amplification and noise squeezing. We coined this amplifier NanoMechanical Bifurcation Amplifier (NMBA).

Phase sensitive amplification is achieved by a homodyne detection scheme, where the displacement detector's output, which has correlated spectrum around the pump frequency, is down converted by mixing with a local oscillator operating at the pump frequency with an adjustable phase. The down converted signal at the mixer's output could be either amplified or deamplified, yielding noise squeezing, depending on the local oscillator phase.

This amplification scheme could be exploited for both signal amplification and noise reduction which could be useful for detection of weak forces. A possible application for our noise squeezing scheme is sensitive mass detection [71], which can be achieved by operating close to the bifurcation point and adjusting ϕ_{LO} to maximize the mass sensitivity.

Studies of a very simple nonequilibrium bistable system - a nearly resonantly driven nonlinear oscillator - have enabled us to observe and investigate the phenomenon of high frequency stochastic resonance. The HFSR phenomenon can be viewed as an example of critical kinetic phenomena in periodically driven nonlinear systems. This

may be used not only to investigate the character and properties of KPT, but also to obtain tunable noise-induced amplification and extremely narrow-band filtering and detection of high frequency signals. HFSR has been demonstrated in a nanomechanical resonator, employing an AM modulation of the pump to modulate the activation barrier between the two stable states. When noise is injected, the resonator's response exhibits noise dependent amplification. SR could be very useful in nanomechanical devices as a mean to implement on-chip mechanical amplification and to increase the signal to noise ratio.

We have measured the nonlinear damping in our device and we have found that it is relatively weak and could be neglected.

There are several possible future research directions.

1) Investigation of light–resonator interaction [79],[80]: light could be used to actuate nanomechanical resonators through optothermal effect or using the radiation pressure. We have measured a dependence of the resonance frequency on the laser power as shown in Fig. 7.1. Here for each laser power (Y axis) we have measured the upward sweep frequency response which is coded in the color of the plot. It is apparent from the figure that as the laser power is increased, the resonance frequency shifts downward.

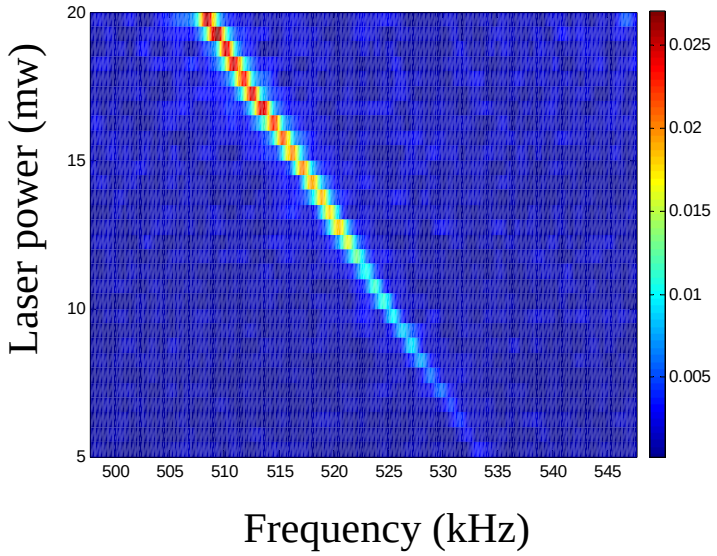

Figure 7.1: The dependence of the resonance frequency on the laser power.

Another interesting application is the cooling of nano/micromechanical resonators by light. This is done using a high finesse nano-opto-mechanical system which couples a mechanical oscillator to an optical cavity field and using dynamical back-action.

2) Investigation of electron beam–resonator interaction: we have found that when the resonator is irradiated by electrons, the beam gets stiffen and the resonance frequency increases by 100 Hz/ min. During two weeks the resonance frequency increased from 500 kHz to 800 kHz. Further work is needed in order to understand the exact mechanism of this phenomenon. This could be used to tune the resonance frequency to a specific value, compensating irregularities generated by the fabrication process.

3) Investigation of chaotic motion for large excitation amplitudes: when the pump and signal are comparable, we have noticed that the frequency response looks continuos instead of having peaks at the mixing product. This could be a sign of a chaotical behavior. The same can happen for increased dc voltage when working closer to the pull in voltage. Investigation of chaos in NEMS is important for the following reasons: a) Characterizing the stability regions of NEMS devices. b) Chaotical motion is important for microfluidics mixers. c) Chaotical motion could be utilized to generate encryption keys.

4) Investigation of higher modes and nonlinear coupling between different modes.

5) Investigation of the nonlinear region using parametric excitation of the device.

6) Investigation of the exact dissipation mechanisms in order to increase the quality factor. A key property of systems based on mechanical oscillators is the rate of damping. In many cases, the sensitivity of NEMS sensors is limited by thermal fluctuations which is related to damping via the fluctuation-dissipation theorem. In general, a variety of different physical mechanisms can contribute to damping, including bulk and surface defects, thermoelastic damping, nonlinear coupling to other modes, phonon-electron coupling, clamping loss etc. NEMS suffer from low quality factors, relative to their macroscopic counterparts. Identifying experimentally the contributing mechanisms in a given system is highly important and challenging.

7) Investigation of the quantum limit of displacement detection. When the resonance frequency get higher towards 1 GHz, the oscillator energy quanta is comparable to the thermal energy in a dilution refrigerator: $\hbar\omega_0 \approx k_B T$. This could lead to new applications using quantum dynamics, *e.g.* entanglement, macroscopic quantum coherence and quantum computation. An interesting possibility is the coupling of a mechanical beam to a single electron transistor (SET) or a superconducting quantum interference device (SQUID).

8) Development of on-chip displacement detection method using electron tunneling between the nanomechanical beam and an adjacent electrode.

Appendix A

Appendix1

This page left empty for Article1 page 1.

This page left empty for Article1 page 2.

This page left empty for Article1 page 3.

This page left empty for Article1 page 4

Bibliography

[1] M.L. Roukes, Phys. World **14**, 2, 25 (2001).

[2] H.G. Craighead, Science **290**, 1532 (2000).

[3] B. Ilic, H. C. Craighead, S. Krylov, W. Senaratne, C. Ober, and P. Neuzil, J. Appl. Phys., **95**, 3694 (2004).

[4] B. Ilic, Y. Yang, K. Aubin, R. Reichenbach, S. Krylov, and H. G. Craighead, Nano Lett. **5**, 925 (2005).

[5] Y. T. Yang, C. Callegari, X. L. Feng, K. L. Ekinci, and M. L. Roukes, Nano Lett. **6**, 583 (2006).

[6] A. Wachter and T. Thundat, Rev. Sci. Instrum. **66,** 3662 (1995).

[7] H. P. Lang„ R. Berger„ C. Andreoli„ J. Brugger, M. Despont, P. Vettiger, C. Gerber, et al., Appl. Phys. Lett. **72**, 383 (1998).

[8] Z. Y. Hu, T. Thundat, and R. J. Warmack, J. Appl. Phys. **90**, 427 (2001).

[9] B. Ilic, D. Czaplewski, H. G. Craighead, P. Neuzil, C. Campagnolo, and C. Batt, Appl. Phys. Lett. **77**, 450 (2000).

[10] J. Fritz, M. K. Baller, H. P. Lang, H. Rothuizen, P. Vettiger, E. Meyer, H. J. Guntherodt, C. Gerber, and J. K. Gimzewski, Science **288**, 316 (2000).

[11] B. Ilic, D. Czaplewski, M. Zalalutdinov, H. G. Craighead, P. Neuzil, C. Campagnolo, and C. Batt, J. Vac. Sci. Technol. B **19**, 2825 (2001).

[12] A. Subramanian, P. I. Oden, S. J. Kennel, K. B. Jacobson, R. J. Warmack, T. Thundat, and M. J. Doktycz, Appl. Phys. Lett. **81**, 385 (2002).

[13] B. Ilic, L. Yang, and H. G. Craighead, Appl. Phys. Lett. **85**, 2604 (2004).

[14] K. L. Ekinci, X. M. H. H, and M. L. Roukes, Appl. Phys. Lett. **84**, 4469 (2004).

[15] M. K. Ghatkesar, V. Barwich, T. Braun, A. H. Bredekamp, U. Drechsler, M. Despont, H. P. Lang, M. Hegner, and C. Gerber, Proc. IEEE Sensors **2004**, 1060 (2004).

[16] Ghatnekar-Nilsson, E. Forsen, G. Abadal, J. Verd, F. Campabadal, F. Perez-Murano, J. Esteve, N. Barniol, A. Boisen, and L. Montelius, Nanotechnology **16**, 98 (2005).

[17] D. Rugar, R. Budakian, H. Mamin, and B. Chui, Nature (London) **430**, 329 (2004).

[18] C.-C. Nguyen, IEEE Trans. Microwave Theory Tech. **47**, 1486 (1999).

[19] A. N. Cleland, *Foundation of Nanomechanics (*Springer, New York*,* 2003*).*

[20] J. S. Aldridge and A. N. Cleland, Phys. Rev. Lett. **94**, 156403 (2005).

[21] A. N. Cleland, New J. Phys. **7** 235 (2005).

[22] K. L. Ekinci and M. L. Roukes, Rev. Sci. Ins. **76**, 061101 (2005).

[23] H. W. Ch. Postma, I. Kozinsky, A. Husain, and M. L. Roukes, Appl. Phys. Lett. **86**, 223105 (2005).

[24] B. Yurke, D. S. Greywall, A.N. Pargellis and P. A. Busch, Phys. Rev. A **51,** (1995) 4211.

[25] A. D. Armour, M. P. Blencowe, and Y. Zhang, Phys. Rev. B **69**, 125313 (2004).

[26] K. L. Turner, S. A. Miller, P.G. Hartwell, N. C. MacDonald, S. H. Strogatz, and S. G. Adams, Nature **396**, 149 (1998).

[27] C. Gui, R. Legtenberg, H. A. Tilmans, J.H. Fluitman and Elwenspoek M, J. Microelectromech. Syst. **7,** 122 (1998)

[28] F. Ayela and T. Fournier, Meas. Sci. Technol. **9**, 1821, (1998)

[29] A. Erbe, H. Krommer, A. Kraus, R. H. Blick, G. Corso, and K. Richter, Appl. Phys. Lett. **77**, 3102 (2000).

[30] M. C. Cross, A. Zumdieck, R. Lifshitz, and J. L. Rogers, Phys. Rev. Lett. **93**, 224101 (2004).

[31] D. Rugar and P. Grütter, Phys. Rev. Lett. **67**, 699 (1991).

[32] D. W. Carr, S. Evoy, L. Sekaric, H. G. Craighhead, and J. M. Parpia, Appl. Phys. Lett. **77**, 1545 (2000).

[33] R. Almog, S. Zaitsev, O. Shtempluck, and E. Buks, Appl. Phys. Lett. **88**, 213509 (2006).

[34] R. Almog, S. Zaitsev, O. Shtempluck, E. Buks, Phys. Rev. Lett. **98**, 078103 (2007).

[35] R. Almog, S. Zaitsev, O. Shtempluck, E. Buks, Appl. Phys. Lett. **90**, 013508 (2007).

[36] S. Zaitsev, R. Almog, O. Shtempluck, and E. Buks, arXiv:cond-mat/0503130 (6 March 2005), submitted to JMEMS.

[37] K. Weisenfeld. J. Stat. Phys. **38**, 1071 (1985).

[38] K. Wiesenfeld, Phys. Rev. A **32**, 1744 (1985).

[39] K. Wiesenfeld and B. McNamara, Phys. Rev. A **33**, 629 (1986).

[40] K. Wiesenfeld and N. F. Pedersen, Phys. Rev. A **36**, 1440 (1987).

[41] E. D. Surovyatkina, Yu. A. Kravtsov, J. Kurths, Phys. Rev. E **72**, 046125 (2005).

[42] Yu. A. Kravtsov and E. D. Surovyatkina, Phys. Lett. A, **319**, 348 (2003).

[43] B. Yurke and E. Buks, arXiv:quant-ph/0505018 (3 May 2005).

[44] H. Krömmer, A. Erbe, A. Tilke, S. Manus, R.H. Blick, Europhys. Lett., **50**, 101 (2000).

[45] S. Savel'ev, A. L. Rakhmanov, F. Nori, Phys. Rev. E **72**, 056136 (2005).

[46] M.I. Dykman, D.G. Luchinsky, R. Mannella, P.V.E. McClintock, N.D. Stein and N.G. Stocks, Phys. Rev. E **49**, 1198 (1994).

[47] I. Siddiqi, R. Vijay, F. Pierre, C. M. Wilson, M. Metcalfe, C. Rigetti, L. Frunzio, and M. H. Devoret, Phys. Rev. Lett. **93**, 207002 (2004).

[48] A. H. Nayfeh and D. T. Mook, *Nonlinear Oscillations* (Wiley, New York, 1979).

[49] L. D. Landau and E.M. Lifshitz, *Mechanics* (Pergamon, Oxford, 1976).

[50] S. D. Senturia, *Microsystem Design* (Kluwer, Norwell, 2001).

[51] R. Benzi, A. Sutera, G. Parisi and A. Vulpiani, SIAM J. Appl. Math. **43**, 565 (1983).

[52] L. Gammaitoni, P. Hanggi, P. Jung and F. Marchesoni, Rev. Mod. Phys. **70**, 223 (1998).

[53] T. Wellens, V. Shatokhin and A. Buchleitner, Rep. Progr. Phys. **67**, 45 (2004).

[54] S. Fauve and F. Heslot, Phys. Lett. A **97**, 5 (1983).

[55] B. McNamara, K. Wiesenfeld, and R. Roy, Phys. Rev. Lett. **60**, 2626 (1988).

[56] R. Rouse, S. Han, and J. E. Lukens, Appl. Phys. Lett. **66**, 108 (1995).

[57] A. D. Hibbs, A. L. Singsaas, E. W. Jacobs, A. R. Bulsara, J. J. Pekkedahl, and F. Moss, J. Appl. Phys. **77**, 2582 (1995).

[58] Baleegh Abdo, Eran Segev, Oleg Shtempluck, and Eyal Buks (2006), arXiv: cond-mat/0606555.

[59] A. Longtin, A. Bulsara, and F. Moss, Phys. Rev. Lett. **67**, 656 (1991).

[60] J. E. Levin and J. P. Miller, Nature **380**, 165 (1996).

[61] R. L. Badzey, and P. Mohanty, Nature **437**, 995 (2005).

[62] H. B. Chan and C. Stambaugh, Phys. Rev. B **73**, 224301 (2006).

[63] E. Buks and M. L. Roukes, Euro. Phys. Lett. **54**, 220 (2001).

[64] E. Buks and M. L. Roukes, Phys. Rev. B **63** 033402 (2001).

[65] E. Buks and M. L. Roukes, JMEMS **11**, 802 (2002).

[66] L. D. Landau and E.M. Lifshitz, *Theory of Elasticity* (Pergamon, Oxford, 1986).

[67] D. Karabacak, T. Kouh, C. C. Huang, K. L. Ekinci, Appl. Phys. Lett. **88**, 193122 (2006).

[68] M. P. Blencowe and M. N. Wybourne, arXiv:cond-mat/9811232 (16 Nov 1998).

[69] B. Yurke, Phys. Rev. A, vol. **32**, p. 300-310 (1985).

[70] R. Movshovich, B. Yurke, P. G. Kaminsky, A. D. Smith, A. H. Silver, R. W. Simon and M. V. Schneider, Phys. Rev. Lett. **65**, 1419 (1990).

[71] E. Buks and B. Yurke, arXiv:quant-ph/0606081 (15 June 2006), to be published in Phys. Rev. E.

[72] C. W. Gardiner and M. J. Collett, Phys. Rev. A **31**, 3761 (1985).

[73] E. Buks and B. Yurke, Phys. Rev. A **73**, 023815 (2006).

[74] Bryant, K. Wiesenfeld and B. McNamara, J. Appl. Phys. **62**, 2898 (1987).

[75] M. I. Dykman and M. A. Krivoglaz, Sov. Phys. JETP **50**, 30 (1979).

[76] P. Jung and P. Hanggi, Phys. Rev. A **44**, 8032 (1991).

[77] M. I. Dykman, M. A. Krivoglaz, and S. M. Soskin, in Noise in Nonlinear Dynamical systems, edited by F. Moss and P. V. E. McClintock (Cambridge University Press, Cambrigde, England, 1989), Vol. 2, p.347.

[78] B. Abdo, E. A.-Segev, O. Shtempluck, and E. Buks, cond-mat/0607628 25 July 2006.

[79] B. Illic, S. Krylov, K. Aubin, R. Reichenbach, and H. G. Craighead, Appl. Phys. Lett. 86, 193114 (2005).

[80] A. Schliesser, P. Del Haye, N. Nooshi, K.J. Vahala, T.J. Kippenberg physics/0611235, accepted for publication by Phys. Rev. Lett.

דינמיקה לא לינארית במתנדים ננומכניים

חיבור על מחקר

לשם מילוי חלקי של הדרישות לקבלת התואר
דוקטור לפילוסופיה

רונן אלמוג

הוגש לסנט הטכניון – מכון טכנולוגי לישראל

טבת 5767 חיפה ינואר 2007

המחקר נעשה בהנחיית דר. אייל בוקס
בפקולטה להנדסת חשמל

אני מודה לקרן ע"ש הנרי גוטווירט, לחברת אינטל, לחברת אפלייד מטריאלס, לקרן הדו-לאומית למדע ישראל-ארה"ב, למכון ראסל ברי לננוטכנולוגיה ולטכניון על התמיכה הכספית הנדיבה בהשתלמותי.

הכרת תודה

ברצוני להודות מקרב לב למנחה שלי, דר' אייל בוקס, אשר האמין בי ותמך בי לאורך המחקר. הדבקות שלו במחקר, בשילוב התובנות הפיזיקליות העמוקות וההנחיה המסורה היוו את הבסיס עליו נבנה מחקר זה.

ברצוני להודות מקרב לב לאולג שטמפלוק על העזרה הרבה בפיתוח ובביצוע תהליכי הייצור ובתכנון המכני של המערכות הניסוייות. כמו כן הנני מודה לברנרד יורקה, עודד גוטליב וחברי קבוצת המחקר שלי – סתו, ערן ובליר על שיחות מועילות ועצות טובות.

ברצוני להודות לכל עובדי המכון למיקרואלקטרוניקה על התמיכה הרבה שהגישו לי במחקר זה.

ברצוני להודות לקבוצת האלקטרואופטיקה של אלכס בקר, בוריס לויט וולדימיר סמולוקובסקי על עזרתם בהקמת מערכת המדידה האופטית.

לסיום, ברצוני להודות לאשתי שרית ולהורי שושנה וניסים על האהבה, התמיכה וההבנה לאורך הדרך הארוכה.

תקציר

מתנדים ננו/מיקרואלקטרומכניים מיועדים לשמש בתפוצה רחבה ליישומים כגון חישה, מיתוג וסינון. במיוחד, מתנדים מכניים אלו יכולים לשמש למדידות רגישות ביותר של כוחות או שינויי מסה. לדוגמא, אחד היישומים המבטיחים בהתקנים אלו הוא מדידה של נוכחות של מולקולות בודדות באמצעות ספיחה שלהן על המתנד תוך כדי שינוי המסה של המתנד ועקב כך גם שינוי תדר הרזוננס של המתנד. ככל שמסת המתנד המקורית קטנה יותר, כך הוא רגיש יותר למדידה בשיטה זו. אחד האתגרים בחיישנים ננומכניים הוא הגדלת רגישות גלאי התנודות ויחס אות לרעש. שיטה אפשרית לענות על צורך זה היא השימוש במנגנון הגברה מכני על השבב עצמו.

בעבודה זו התמקדנו בחקר הדינמיקה הלא לינארית בהתקנים אלו ובפיתוח שיטות הגברה מכנית חדשות המנצלות את התחום הלא לינארי. שתי שיטות למנגנון הגברה מכני נחקרו. האחת משתמשת בעובדה כי מערכת לא לינארית הנמצאית לפני ביפורקציה (שינוי תחומי היציבות של המערכת) רגישה מאוד לתנודות קטנות. השיטה השניה משתמשת בתופעה הידועה בשם Stochastic Resonance שבה רעש יכול לתרום להגבר במערכת לא לינארית ביסטבילית.

בשיטה הראשונה חקרנו ניסיונית ותיאורטית הגבר מכני ודחיסת רעש במתנד ננומכני לא לינארי הרוטט תחת אילוץ של כוח חיצוני חזק ליד נקודת הביפורקציה של ההתקן, שהיא במקרה זה המעבר של המערכת לביסטביליות האופיינית למתנד Duffing. במתנד Duffing, האי לינאריות היא מסדר ראשון, ונוצרת ע"י כוח אלסטי לו יש תלות מסדר שלישי בתזוזה. בעבודה זו השתמשנו לראשונה בהגבר מבוסס על ביפורקציה במתנד ננומכני והדגמנו הגבר גבוה, הגברה תלוית פאזה ודחיסת רעש. הגבר תלוי פאזה מושג בעזרת הכפלת האות החשמלי ביציאה של ההתקן באות חיצוני בתדר הכוח המאלץ ובעל פאזה נשלטת. בצורה זו ניתן לשלוט על הגבר או הנחתת האות לפי פאזת האות החיצוני.

בשיטת ההגברה השניה, חקרנו את תופעת ה Stochastic Resonance במתנד ננומכני לא לינארי בתחום הביסטביליות. המתנד מכוון לנקודת עבודה בה קצבי הקפיצות התרמיות בין המצבים זהה. במצב זה מפעילים איפנון אמפליטודה של הכח המאלץ. כאשר מוסיפים רעש למערכת, ניתן להגיע למצב שבו עבור רעש אופטימלי, המתנד יעבור ממצב יציב אחד למצב היציב השני כל חצי מחזור של האפנון ומתקבל הגבר תלוי רעש בו יחס האות לרעש מקבל מקסימום מקומי עבור ערך רעש מסויים.

נוסף לניסויים אלו, עסקנו גם בדיסיפציה לא לינארית. פיתחנו ביטוי מתמטי לאיבר הדיסיפציה הלא לינארית ומדדנו אותו ניסויי. לגורם זה חשיבות רבה בקביעת הדינמיקה של ההתקן, אך במקרה שלנו היה ניתן להזנחה.

המתנד הננומכני עשוי מקורת זהב AuPd הרתומה בשני קצוותיה והמאולצת לרטיטה ע"י אלקטרודה שכנה בעזרת צימוד קיבולי. אורך הקורה 100µm, רוחבה 0.5µm ועובייה 0.25µm. התנודה הנמדדת היא תנודת האופן הבסיסי של הקורה במרכז הקורה. לקורה מקדם טיב (Q factor) של כ 2000 (בואקום) ותדר רזוננס של כ 500kHz .

העבודה כללה פיתוח תהליך מתאים לייצור ההתקנים, הקמת מערכת מדידה אופטית בואקום (תא של מיקרוסקופ אלקטרוני) למדידת התנודות המכניות, ביצוע מדידות וניתוחם ופיתוח נושאים תיאורטיים.

ההתקן מיוצר באמצעות תהליכי Bulk micromachining ביחד עם כתיבה בקרן אלקטרונים. התהליך מתחיל מפיסת סיליקון המצופה בשני צדדיה בSi_3N_4 בעובי 100nm. בשלב הראשון מבצעים תהליך פוטוליטוגרפיה בו פותחים ב Si_3N_4 פתח ריבועי. בשלב השני מבצעים איכול רטוב אנאיזוטרופי של KOH בו מקבלים ממברנה של Si_3N_4 בצידה השני של הפיסה, המשמשת כשכבת הקרבה להתקן. בשלב השלישי מצפים את הממברנה ב PMMA וכותבים את תבנית ההתקן באמצעות ליטוגרפיית קרן אלקטרונים (EBL). לאחר הכתיבה מבצעים פיתוח של ה PMMA שבו מוסרת שכבת ה PMMA שהיתה חשופה לקרן האלקטרונים. בשלב הרביעי מבצעים נידוף של AuPd . לאחר הנידוף מבצעים Lift-off שמשאיר את תבנית הזהב בצורת ההתקן על הממברנה. בשלב האחרון מבצעים שחרור של ההתקן באמצעות איכול של הממברנה בפלזמת Electron Cyclotron Resonance (ECR) המבוסס על תערובת גזים CF4/O2.

מדידת התנודות נעשית בתוך תא ואקום של מיקרוסקופ אלקטרוני Scanning Electron Microscope (SEM). בניסויים הראשונים השתמשנו בקרן האלקטרונים במצב Spot כדי למדוד את התנודות, כאשר הקרן פוגעת בשפת ההתקן והתנודה של ההתקן גורמת לאפנון האות המתקבל בגלאי האלקטרונים המשניים. לאחר ביצוע מספר מדידות בטכניקה זו, גילינו שקרן האלקטרונים הפוגעת בהתקן גורמת להקשחתו ותדר הרזוננס גדל בקצב של 100Hz/min. מסיבה זו עברנו לעבוד בשיטת מדידה אופטית שהיתה יציבה הרבה יותר. לצורך כך התקנו סיב אופטי (שבקצהו עדשה) בתוך התא כאשר הקורה הרוטטת מוצבת באזור הפוקוס של הסיב. האור הפוגע בקורה מאופנן ע"י תנודות הקורה ומוחזר לתוך הסיב. הסיב מוזן באמצעות לייזר הפועל באינפרה אדום באורך גל 1.55µm ובהספק 20mw. הלייזר והגלאי האופטי מחוברים דרך Optical coupler לסיב כך שאור הלייזר נכנס לסיב והאור החוזר מגיע לגלאי.

לעבודה זו מספר כיווני המשך מחקר אפשריים.

כיוון מחקר ראשון הוא באינטראקציה בין קרן האלקטרונים לבין הקורה. קרן האלקטרונים גורמת להקשחה של הקורה. יש להבין המנגנון הגורם להקשחה. ניתן לחשוב על יישומים מעניינים לתכונה זו לצורך כוונון תדרי תהודה של התקנים מסוג זה. כיוון מחקר שני הוא האינטראקציה בין קרן האור לקורה. קרן האור יכולה לשמש לא רק למדידה כי אם גם להפעלת עירור תרמי (כמנגנון אקטואציה). אנו הבחנו באפקט מעניין שבו תדר הרזוננס היה תלוי בהספק הקרינה, כך שככל שההספק היה גבוה יותר, תדר הרזוננס היה נמוך יותר.

כיוון מחקר שלישי הוא חקר מנגנוני איבודי האנרגיה (דיסיפציה) של הקורה. חקר זה חשוב מאד לצורך קבלת מקדם טיב גבוה יותר להתקנים אלו.

כיוון מחקר רביעי הוא חקר התחום הכאוטי. בעירור הקורה ע"י סכום שני אותות קרובי תדר באמפליטודה גבוהה, ספקטרום המוצא המתקבל נראה כרציף, דבר המעיד על אפשרות של תגובה כאוטית.

כיוון מחקר שישי הנו חקר התחום הקוונטי. עבור טמפרטורות נמוכות (10mK) המושגות במקרר dilution ניתן להגיע למצב בו האנרגיה התרמית הינה ברת השוואה לקוונט האנרגיה של המתנד הננומכני, כך שההתנהגות הקוונטית של המתנד כבר אינה זניחה ויכולה לתת את אותותיה.

נושא מחקר נוסף הינו אינטראקציה לא לינארית בין מודים שונים.

מבנה העבודה הינו כדלקמן: הפרק הראשון הינו מבוא לתופעות הנחקרות בתזה. הפרק השני מתאר את ההתקן, תהליך הייצור ומערכת המדידה. הפרק השלישי מציג את התאוריה בנושא הגבר ליד נקודת הביפורקציה. הפרק הרביעי מציג את מדידת ההגבר ליד נקודת הביפורקציה, הפרק החמישי מציג מדידת הגבר תלוי הפזה ודחיסת רעש והפרק השישי מציג את מדידת תופעת ה Stochastic Resonance. הפרק השביעי והאחרון מציג סיכום וכיווני מחקר עתידיים והנספח מציג מאמר בנושא הדיסיפציה הלא לינארית.